AFRL-RY-WP-TR-2019-0184

SPARSE APERTURE MEASUREMENT IN A NON-IDEAL SEMI-ANECHOIC CHAMBER

Joe J. Vinci
University of Dayton

SEPTEMBER 2019
Final Report

AIR FORCE RESEARCH LABORATORY
SENSORS DIRECTORATE
WRIGHT-PATTERSON AIR FORCE BASE, OH 45433-7320
AIR FORCE MATERIEL COMMAND
UNITED STATES AIR FORCE

REPORT DOCUMENTATION PAGE

Form Approved
OMB No. 0704-0188

1. REPORT DATE *(DD-MM-YY)*	2. REPORT TYPE	3. DATES COVERED *(From - To)*
September 2019	Thesis	18 June 2019 – 18 June 2019

4. TITLE AND SUBTITLE
SPARSE APERTURE MEASUREMENT IN A NON-IDEAL SEMI-ANECHOIC CHAMBER

5a. CONTRACT NUMBER
FA8650-17-C-1026

5b. GRANT NUMBER

5c. PROGRAM ELEMENT NUMBER
62204F/63203F/61102F

6. AUTHOR(S)
Joe J. Vinci

5d. PROJECT NUMBER
7622/665A/3002

5e. TASK NUMBER
N/A

5f. WORK UNIT NUMBER
Y1LB

7. PERFORMING ORGANIZATION NAME(S) AND ADDRESS(ES)

University of Dayton
300 College Park Drive
Dayton, OH 45469

8. PERFORMING ORGANIZATION REPORT NUMBER
AFRL-RY-WP-TR-2019-0184

9. SPONSORING/MONITORING AGENCY NAME(S) AND ADDRESS(ES)

Air Force Research Laboratory
Sensors Directorate
Wright-Patterson Air Force Base, OH 45433-7320
Air Force Materiel Command
United States Air Force

Defense Advanced Research Projects Agency (DARPA)
675 North Randolph Street
Arlington, VA 22203

Air Force Office of Scientific Research Public Affairs (AFOSR)
875 North Randolph Street, Suite 325, Room 3112
Arlington, VA 22203

10. SPONSORING/MONITORING AGENCY ACRONYM(S)
AFRL/RYWE

11. SPONSORING/MONITORING AGENCY REPORT NUMBER(S)
AFRL-RY-WP-TR-2019-0184

12. DISTRIBUTION/AVAILABILITY STATEMENT
Approved for public release; distribution is unlimited.

13. SUPPLEMENTARY NOTES
PAO case number 88ABW-2019-3048, Clearance Date 18 June 2019. This work is in partial fulfillment of the requirements for the degree of Master of Science in Electrical Engineering at the School of Engineering of the University of Dayton. Report contains color.

14. ABSTRACT

Antenna aperture technology is a critical component of any radar system. The aperture of many early radar systems was composed of a single antenna [33]. As technology advanced, single antenna apertures were replaced by electronically steered arrays for their ability to rapidly steer beams [2]. With the growth in processing capabilities, digitization at every element is becoming increasingly possible. With digitization at every element, array elements no longer must be co-located, and instead can be arbitrarily sparse allowing increased flexibility in resulting beam patterns. This capability is of extreme interest in recent years [4] [21] [12] [17]. Key challenges in building arbitrarily sparse arrays is their calibration and measurement. Sparse array calibration becomes challenging in due to the nature of each system being completely independent. Each independent system has its own RF chain including oscillators, amplifiers, exciters and receivers which must be considered during calibration. In some sparse arrays, spatial relationship between antennas is not necessarily fixed. In addition, capturing the radiation patterns of sparse arrays is challenging due to the size of the effective array aperture imposing a need for large chambers to reach the far field.

15. SUBJECT TERMS
antenna aperture, sparse aperture measurement

16. SECURITY CLASSIFICATION OF:			17. LIMITATION OF ABSTRACT:	18. NUMBER OF PAGES	19a. NAME OF RESPONSIBLE PERSON (Monitor)
a. REPORT	b. ABSTRACT	c. THIS PAGE			Reginald Cooper
Unclassified	Unclassified	Unclassified	SAR	76	19b. TELEPHONE NUMBER *(Include Area Code)* N/A

Sparse Aperture Measurement in a Non-Ideal Semi-Anechoic Chamber

Thesis

Submitted to

the School of Engineering of the

UNIVERSITY OF DAYTON

In Partial Fulfillment of the Requirements for

The Degree of

Master of Science in Electrical Engineering

By

Joe J. Vinci, B.S.

UNIVERSITY OF DAYTON

Dayton, Ohio

May, 2019

Sparse Aperture Measurement in a Non-Ideal Semi-Anechoic Chamber

Name: Vinci, Joe John

APPROVED BY:

Michael C. Wicks, Ph.D. Advisor Committee Chairman Electrical & Computer Engineering Professor	Robert Penno, Ph.D. Committee Member Electrical & Computer Engineering Professor
Guru Subramanyam, Ph.D. Committee Member Electrical & Computer Engineering Professor	Andrew Kordik, M.S. Committee Member Electrical & Computer Engineering Teaching Fellow
John Weber, Ph.D. Associate Dean School of Engineering	Eddy Rojas, Ph.D. Dean, School of Engineering & Wilke Distinguished Professor

ABSTRACT

Sparse Aperture Measurement in a Non-Ideal Semi-Anechoic Chamber

Name: Vinci, Joe John
University of Dayton

Advisor: Dr. Michael C. Wicks

Antenna aperture technology is a critical component of any radar system. The aperture of many early radar systems was composed of a a single antenna [33]. As technology advanced, single antenna apertures were replaced by electronically steered arrays for their ability to rapidly steer beams [2]. With the growth in processing capabilities, digitization at every element is becoming increasingly possible. With digitization at every element, array elements no longer must be co-located, and instead can be arbitrarily sparse allowing increased flexibility in resulting beam patterns. This capability is of extreme interest in recent years [4] [21] [12] [17].

Key challenges in building arbitrarily sparse arrays is their calibration and measurement. Sparse array calibration becomes challenging in due to the nature of each system being completely independent. Each independent system has its own RF chain including oscillators, amplifiers, exciters and receivers which must be considered during calibration. In some sparse arrays, spatial relationship between antennas is not necessarily fixed. In addition, capturing the radiation patterns of sparse arrays is challenging due to the size of the effective array aperture imposing a need for large chambers to reach the far field.

This thesis develops an in-situ calibration technique for arbitrarily sparse arrays, a measurement technique in non-ideal semi-anechoic chamber, and validates the experimental results against industry standard electromagnetic modeling and simulation tools.

TABLE OF CONTENTS

LIST OF FIGURES

Figure **Page**

CHAPTER 1

Introduction

Antennas are the mode by which we perform modern communication [7]. The first antenna test was performed by Marconi in 1901 where he demonstrated that information could be transferred wirelessly over a distance of 3,500 km [18]. Since then, the race for advancing antenna design has continued.

Antennas have a wide variety of performance metrics, of principle interest here is the frequency of operation and beam pattern. The frequency of operation is defined by the size and shape of the conductive material in the antenna. For example, in the design of dipole antennas, the ideal lengths of the arms is $\frac{\lambda}{4}$ where λ is the wavelength of the frequency of operation. The reason for this is so that across the total length of the antenna $\frac{\lambda}{2}$, the point of highest energy in the wave is on one side of the antenna and the point of lowest energy is on the other. This energy difference causes higher current flow between the two terminals of the antenna. An antennas shape can be designed to optimize interaction with a range of frequencies. This range is called the bandwidth of the antenna. The beam pattern of an antenna described the level of interaction it has with the electromagnetic field compared to an isotropic source [8]. An isotropic source describes a theoretical radiating element which radiates the same energy level in all directions. An antenna's beam pattern shows how it differs from

isotropic at different angles. The beam pattern is also influenced by the shape and size of the antenna. The beam pattern's power is typically plotted in decibels (dB)[8].

When more than one antenna is used for transmission or reception, they form an antenna array and has another complete set of properties. The number of elements as well as the spacing between elements, frequency of operation and signal phase at each element form the definition of the array factor. The array factor and the beam pattern of an element in the array combine to form the beam pattern of the array. The position of the elements can be spaced evenly along a line for a linear array, evenly over a surface for a planar array, or in a volume for a volumetric array. Depending on the configuration of antenna elements, the array factor heavily modifies the resulting beam pattern of the array. When the antennas in an aperture are spaced significantly apart, for example much further than the wavelength of the operating frequency, they become a sparse array [26].

The advantage of sparse arrays is to maintain some of the strengths garnered by large uniform arrays while reducing the number of elements required in the array. This leads to the development of large arrays. This was not previously possible due to the required precise control of the signals at each element and the limitations of hardware in antenna array systems. However, with the emergence of the software defined radio (SDR) digitization at every element allows for control of the signal energizing each element without physical connections between elements. Thus, sparse array elements can be placed at a much greater variety of positions and previously untested functions of sparse arrays can be performed.

However, SDRs are not designed with the phase precision required by a sparse array system. This is a result of the design constraint which details that the placement

of each element controlled by an SDR is not precise. A solution to this is to perform an in-situ calibration of all elements in the array. The calibration involves each element transmitting a unique and orthogonal signal which is reflected off a target and received. The received signal is then processed such that the signals from each element can be identified. With this result, the signals can be adjusted, such that the signals from each element coherently hit the target. Additional sparse array and radar techniques can then be performed.

Further challenges exist which prevent the in-situ calibration from operating without error. SDRs are known to experience ADC aperture jitter which leads to inconsistent phase measurements [32]. Also while set to the same value, the frequencies across separate SDRs vary with enough significance to disrupt the calibration by producing inconsistent phase values. A solution to this problem is to use a reference clock for each SDR. The challenges with this are the positioning limitations of partially connected array elements or configuring GPS clocks for each element.

The objective of this thesis is to investigate the beam patterns of sparse arrays in a non-ideal environment using an SDR with an in-situ calibration. This measured result is compared to a simulated result using FEKO with identical antenna design and placement. The following work first describes the fundamentals of antennas, arrays and sparse arrays, followed by a description and explanation of measurement facilities and SDRs. The process of calibration is introduced and explained, as well as a test of the stability of the coherent signals. A description of the lab setup and measurements is provided followed by the simulation setup and acquired data. The measured data and simulated data are then compared and evaluated. Finally, the further work is posed.

CHAPTER 2

Fundamentals

2.1 Antenna Fundamentals

Antennas are structures which are designed to interact with the electromagnetic field. This interaction is the result of the shape and size of the antenna as well as the signal used to energize it. Current flowing through the antenna material induces an electromagnetic field which in turn propagates through space. Inversely, due to the principle of reciprocity [**?**], an antenna in the presence of an electromagnetic field with certain performance characteristics will develop a current flow in the conducting material. Some defining performance characteristics of antennas which are relevant to this research are gain and frequency response. The gain of an antenna represents the amount of energy radiated in a single direction versus an isotropic source. A plot showing the gains in all directions reveals the antenna's radiation pattern. These can be plotted in 3D or in 2D showing either the antenna's azimuth pattern or elevation pattern. Figure 2.1 shows an example of a 2D antenna pattern.

It is described in [35] that the gain of an antenna is proportional to and highly dependent on the effective aperture of the antenna. Equation 2.1 shows this relationship.

$$G_r(\theta, \phi) = \frac{4\pi}{\lambda^2} A_{e,r}(\theta, \phi) \tag{2.1}$$

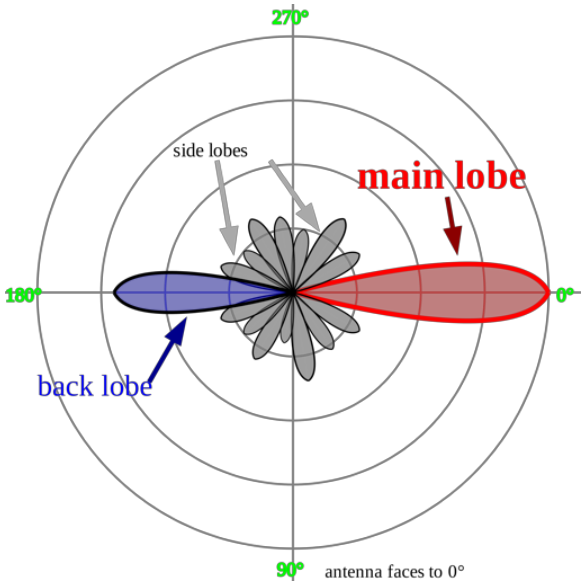

Figure 2.1: 2D Antenna Radiation Pattern

where G_r is the gain at the elevation angle θ and azimuthal angle ϕ, $A_{e,r}$ is the effective area of the antenna and λ is the wavelength. The wavelength is defined by $\lambda = \frac{c}{f}$ where c is the speed light, and f is the frequency of operation.

The frequency response of the antenna shows the frequency band in which the antenna optimally operates. Meaning the antenna experiences higher gain when in the presence of an electromagnetic field energized at a frequency within the antenna's frequency response. Likewise, the antenna will induce an electromagnetic field of higher energy if the signal used to energize the antenna is within the frequency response of the antenna. The frequency response of the antenna is usually provided by the manufacturer. If it is not provided or if the antenna has not been officially tested, the frequency response can be obtained by use of radio frequency (RF) equipment. The antenna can be connected to a network analyzer and be energized by a signal which sweeps through a range of frequencies and measures the energy at

each frequency. The radiation pattern and frequency response of the antenna can be measured at the same time by use of the network analyzer inside a measurement chamber and measuring the frequency response at all directions of the antenna. This is a typical practice in the antenna design industry.

Another important antenna characteristic related to both the size of the antenna and the frequency response is the size of the near and far field. The near field can be divided into two zones. The non-radiative (reactive) zone and the radiative (Fresnel) zone. The reactive zone starts at the surface of the antenna and extends to $R = \frac{\lambda}{2\pi}$. The reactive field interacts with antenna components and loses strength with distance at a significant rate. Past this region starts the near field radiative zone which extends out to the start of the far field. Likewise, the radiative zone is the distance by which changes in the distance from the antenna alters the radiation pattern and relative gain [1].

The far field is a radial distance from the antenna where a radiating signal can be approximated by a plane wave. The formal name of this principle is the Far Field Approximation and is defined by Equation 2.2.

$$R > \frac{2D^2}{\lambda} \tag{2.2}$$

R is the radial distance from the antenna, D is the aperture size of the antenna and λ is the wavelength of the frequency of transmission. If a measurement made on an antenna satisfies the Far Field Approximation, then the transmitted waveform can be treated as a plane wave propagating tangential to the transmitting antenna [35]. If R does not meet these conditions, then the measurement device is in the near-field of the transmitting antenna [**?**] [3]. Also, two conditions must be met in order to use this approximation. $R >> D$ and $R >> \lambda$, meaning that the distance from the antenna

to the start of the far field must be sufficiently larger than the effective aperture of the antenna, D, and the wavelength being transmitted, λ [31].

The advantage of high gain associated with large effective aperture brings forth the challenge of designing systems to accommodate large antennas. A solution to this problem is to use multiple antenna elements arranged in an array which results in a larger effective aperture than a single element.

2.2 Arrays

Arrays were first used to replace single element antennas for military radar applications [2]. An antenna array uses multiple antenna elements arranged in a pattern to form one large antenna. This pattern can be linear in which the elements are positioned along a line, planar in which the elements are positioned on a 2D plane and volumetric in which the elements are placed within a 3D space. In typical arrays, the spacing between the elements is uniform and does not exceed $\frac{\lambda}{2}$. The reason for this is to prevent exceeding one Nyquist interval spatially which gives rise to grating lobes in the radiation pattern [26]. It is also important to note that typical arrays use identical elements. The use of non-identical elements in an array will not be examined in this work.

The radiation pattern of the array is governed by the radiation pattern of a single element in the array and the array factor. The array factor for a linear array can be described by Equation 2.3 in [35].

$$f(\psi) = \sum_{n=0}^{N-1} a_n e^{j\psi} \tag{2.3}$$

where a_n is the amplitude applied to each element n, and $\psi = k_0 d cos\theta - \alpha$ describes the element position and phase at each element. $k_0 = \frac{2\pi}{\lambda}$ represents the wavenumber,

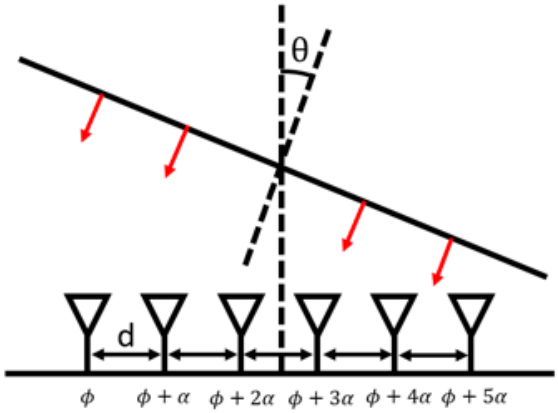

Figure 2.2: Illustration of Array Parameters and Incident Waveform

d is the spacing between elements and is assumed to be equal in a linear array, θ represents the direction of the propagating or incident waveform with respect to the orientation of the linear array and α is the phase progression between elements. An advantage of using individual elements to form an array is the ability to control parameters of the signal energizing each element. As such, the amplitude and phase of the signal energizing each element can be controlled. This is especially beneficial because the array factor can be adjusted without physical changes being made to the array such as varying the spacing between elements or the orientation of the array. The array factor influences the radiation pattern of the array by Equation 2.4 as described in [35].

$$E_{tot}(\theta, \phi) = E_{el}(\theta, \phi) f(\psi) \tag{2.4}$$

where E_{tot} represents the radiation pattern of the array in all directions θ and ϕ, and E_{el} is the radiation pattern of a single element in the array. Figure 2.2 helps illustrate the parameters used to determine the array factor. Adjustment of the phase difference between elements α to change the direction of the wave front θ is a technique called

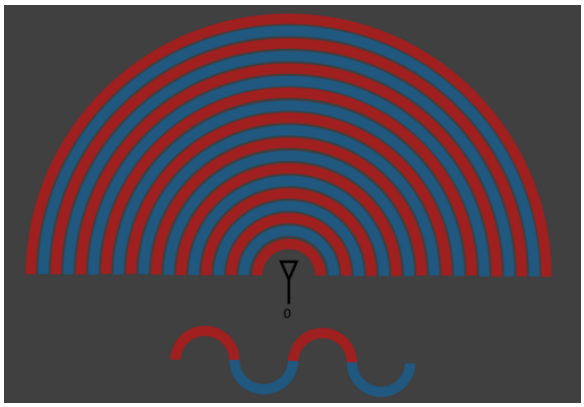

Figure 2.3: Single Semi-Isotropic Element

beam forming or beam steering. Beam forming is advantageous for radar applications due to the ability to rapidly direct the main lobe of an array in a range of directions without physical movement of the antenna. There are several physical limitations of rapidly steering a non-electronically steered antenna including torque demands and structure wear. Electronically steered arrays are far better suited for this purpose. A disadvantage of electronically steered arrays is the maximum Field of View (FOV). For linear and planar arrays, this value is 120° [36]. However, this is usually overcome by placement of more arrays in different orientations or by physical movement of the array as in gimballed arrays in the nose of some military aircraft. Figure 2.3 and 2.4 illustrate beam forming in a different manner.

The red and blue partially transparent semicircles represent higher and lower signal parts of a sine wave radiated from an isotropic antenna. When semicircles of the same color overlap, they appear to have greater contrast as a result of the two overlapping 50% transparent lines. When different colors overlap, the shared region appears dark as a result of the red and blue mixing. The background is

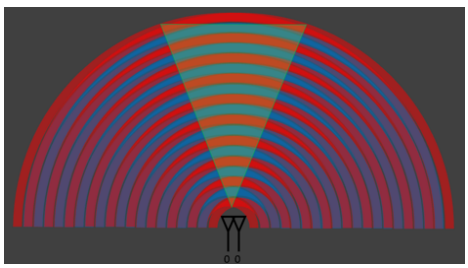

(a) $\frac{\lambda}{2}$ Spacing, 0 Phase Shift

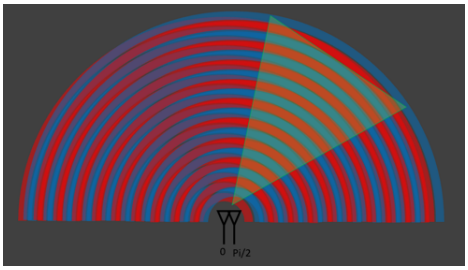

(b) $\frac{\lambda}{2}$ Spacing, $\frac{\pi}{2}$ Phase Shift

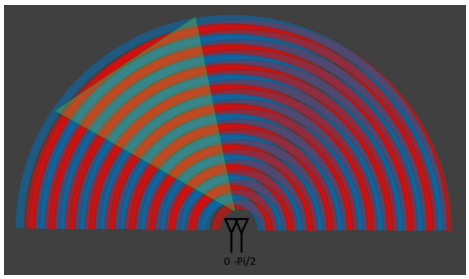

(c) $\frac{\lambda}{2}$ Spacing, $-\frac{\pi}{2}$ Phase Shift

Figure 2.4: Beam Forming Illustrated using Phase Shifted Semi-Isotropic Elements

chosen to be grey to discriminate between the darker and higher contrast regions. The high contrast, or brighter regions and the darker regions represent the pattern of constructive and deconstructive interference respectfully of the two antennas. Figure 2.4a shows the two antennas spaced $\frac{\lambda}{2}$ apart with no phase difference. The pattern is no longer purely isotropic, but narrowed forward. This beam would have double the energy in the brighter areas and little to no energy in the dark areas simply because another identical antenna has been added. If the phase of one of the antennas is shifted, the beam is directed to an angle as seen in Figure 2.4b. The physical array has not moved but the phase of the signal from the right element is delayed by $\frac{\pi}{2}$, thus steering the beam to the right. Figure 2.4c shows the effect of phase shifting the right element by $-\frac{\pi}{2}$, steering the beam to the left.

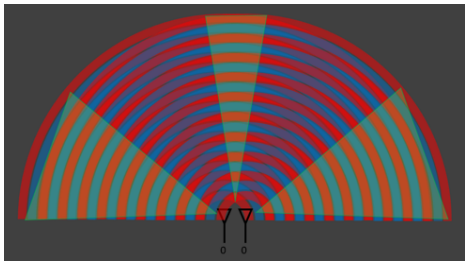

(a) λ Spacing, 0 Phase Shift

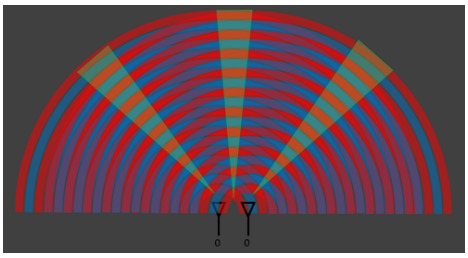

(b) $\frac{3\lambda}{2}$ Spacing, 0 Phase Shift

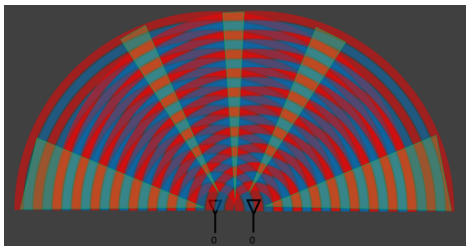

(c) 2λ Spacing, 0 Phase Shift

Figure 2.5: Grating Lobe Appearance with Element Separation

2.3 Sparse Arrays

When the spacing between antenna elements exceeds $\frac{\lambda}{2}$, grating lobes begin to form in the beam pattern. However, the levels of the grating lobes can be controlled by various techniques for spacing the array elements. An array which uses this principle is called a sparse array. Optimal positioning of array elements can yield greater main lobe gain using less elements within the same space than a uniform array with $\frac{\lambda}{2}$ element spacing. The appearance of grating lobes as the spacing between antenna elements can be represented in a similar manner to Figure 2.4. The same isotropic elements are used with no phase shift between elements. Only the spacing between elements is adjusted with the results in Figure 2.5. In subfigure 2.5a, the elements are spaced λ, or one whole wavelength, apart. By comparison to subfigure 2.4a on Figure

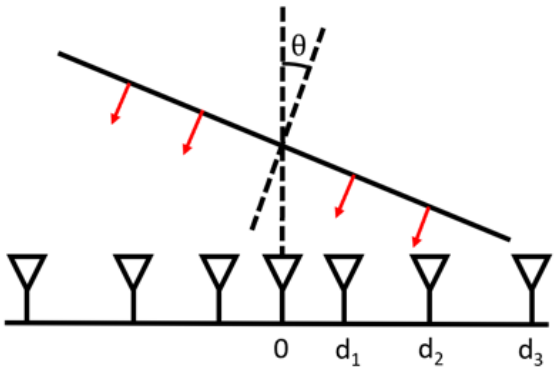

Figure 2.6: Illustration of Sparse Array Parameters and Incident Waveform

2.4 the main beam appears to narrow while a pair of grating lobes emerge. As the spacing increases in subfigures 2.5b and 2.5c more grating lobes appear and converge toward the center. The effect of increased element spacing introducing grating lobes to the radiation pattern is relevant to the results of this thesis.

The objective of sparse array design is to reduce the grating lobe levels using optimal element spacing. The techniques described in [22] give a method for calculating element positioning in a linear sparse array. Figure 2.6 illustrates the array parameters for a sparse array. The array factor in Equation 2.3 is modified to allow for non-uniform element positioning while removing the phase shifting component α shown in Equation 2.5.

$$f(\psi) = 2\sum_{n=1}^{[N/2]} a_n cos(k_0 d_n cos\theta) \tag{2.5}$$

where $[N/2]$ is an integer no less than N/2. Continuing to follow the procedure used in [22], it is now assumed that all elements are equally spaced in some range $-x_m$ to x_m with spacing Δd Equation 2.5 can be written in matrix form

$$[f]_{mx1} = [A]_{mxn}[r]_{nx1} \tag{2.6}$$

where m is the number of sampled antenna radiation patterns, and n is an integer greater than $\frac{2x_m}{\delta d}$. f is the set of array factors $[f(\psi_N)]^T$, r is the set of $[a_n]^T$, and $A_{ij} = 2a_n cos(kd_n cos\theta_j)$. The principle is that some elements in this array are not required to radiate energy while the array produces the same array factor. Thus, certain amplitude values a_n can be set to zero and the element can be removed. Determining these elements requires casting the array as a convex minimization problem where the a_n values are minimized iteratively such that Equation 2.6 is satisfied. Thus, the same array factor remains which antenna elements can be removed from the array.

This is only one such method in reducing the number of elements called compressive sensing [22]. Several other methods will be mentioned here such as particle swarm optimization (PSO) used in [34]. The concept of PSO is that every possible solution in a randomly generated population is chosen as a particle. All the particles are run through multiple fitness tests which change each particle's position with respect to the environment and other particles. The error for each particle is defined and the particle with minimum error has the optimal parameters for the sparse array. Another technique uses Taylor line source distribution for element spacing [30]. It considers regions of equal area under a peaked curve to place the elements, using this area as weightings for position. This method proves to be an improvement to uniform array spacing with a procedure that does not require significant computation. The last method that will be referenced in this thesis is synthesis using a differential evolution algorithm [19]. By use of a search technique looking to diminish sidelobe levels and determining the characteristics of improved versions, the ideal element positions can be determined. This is similar to the procedure of a genetic algorithm.

With these advanced grating lobe suppression techniques sparse arrays can achieve the same spatial advantages of non-sparse arrays of the same geometries.

2.4 Antenna Measurement Facilities

Ideally, antennas would be measured in free space with no surrounding objects which could interfere with the antenna signal. This is nearly impossible due to antenna mounting arrangements and spatial challenges. An outdoor range is a partial solution to this problem. For the setup, a transmission antenna is placed at a distance, satisfying the far field approximation in Equation 2.2, from a receive antenna or reflecting surface. The signal from the transmission antenna radiates toward the receive antenna. The outdoor range at Wright Patterson Air Force Base is shown in Figure 2.7 obtained from wpafb.af.mil [5]. Scatter from the antenna tower is

Figure 2.7: The Outdoor Range at Wright Patterson Air Force Base (wpafb.af.mil)

present but is minimal compared to the energy directed at the receive antenna. The disadvantage of outdoor ranges is that they require large startup construction costs

both in finances and in time. Another disadvantage is the equipment used in the outdoor range must be made weather proof to protect the expensive equipment. Having bad weather also means that operation of the range is weather dependent. Atmospheric conditions between the antenna elements in the range can significantly reduce the quality of the signal in certain frequency bands. A potential advantage to this is that measurements can be taken in poor conditions to determine the performance of the antennas in this environment.

A compact range is an indoor chamber which uses a large reflector to mimic a far field wave front. Unlike outdoor ranges, the maximum dimensions of the chamber may not allow for the transmission and receive elements to be placed such that the receive element is in the far field based on the frequency of operation. The solution offered by compact ranges is to direct the energy towards a parabolic reflector which collimates the spherical transmitted wave into a planar wave front. Figure 2.8 illustrates this principle. There exist several types of compact ranges. The single offset reflector

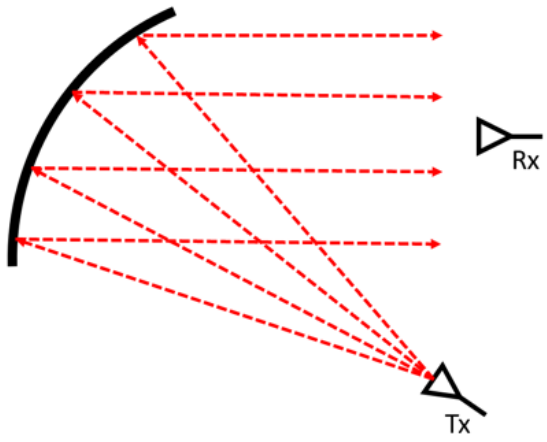

Figure 2.8: Principles of a Compact Chamber

contains only one reflective dish as described above, while the dual cylinder reflector uses two parabolic cylinders to convert the spherical wave into a cylindrical wave. The Dual Cassegrain reflector, the Dual shaped reflector, the Paneled millimeterwave reflector and the Lens type compact range are all examples of different configurations of compact ranges [25].

However, because the chamber is indoor, scattering of the electromagnetic waves off mounting devices, walls or any other surface is problematic for capturing data. The objective of the compact range is to simulate a plane wave impacting the receive element or test object without interference from nearby reflectors. To subdue the undesired scattering, every surface in the indoor chamber, for the exception of the antenna elements or test objects and the parabolic reflector, is covered in absorber material. This material is described in greater detail when describing the next type of chamber, anechoic chambers.

An anechoic chamber is an indoor antenna measurement chamber designed with the intention of reducing unintended electromagnetic scattering. Typically, an anechoic chamber uses absorber material on all surfaces. According to [35], all surfaces on the chamber must be covered by absorber which meets the lowest frequency requirements. The thickness of the absorber material, which is the tip to base dimension of the pyramids, should be at least two wavelengths of the lowest frequency of operation [16].

The Mumma Lab at the University of Dayton uses a semi anechoic chamber. Due to building constraints, the Mumma lab chamber does not cover all surfaces and is thus semi anechoic. There are objects and surfaces in the chamber which would scatter energy and disrupt the quiet zone (QZ). The QZ is a volume in the

chamber in which the conditions during antenna measurement resembles ideal free space with minimal unintended scattering. The absorber material used in anechoic chambers was not commercially produced until the mid-1950s [11]. The material itself is carbon coated and pyramidal in shape. This type of absorber is capable of attenuating incoming signals less than -60 dB. Meaning that a signal at 0 dB directed toward the absorber would reflect with a signal power of only -60 dB. Figure 2.9 shows an image of this type of absorber. The objective of the design is for a portion

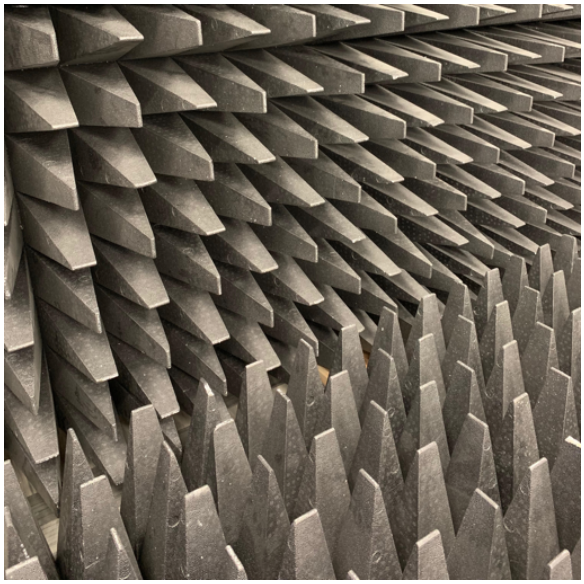

Figure 2.9: Pyramidal Absorber in the Mumma Lab

of the energy of the transmitted waves, propagating incident to the sheet of absorber, to be absorbed by the carbon loaded surface. The portion of energy not absorbed by the first interaction is reflected toward adjacent absorber cones where the wave is partially absorber and reflected again. This repeats, degrading the power of the wave as it continues to interact with the absorber material. Thus, minimal energy is

reflected back into the chamber. This is illustrated in Figure 2.10. Hemming provides

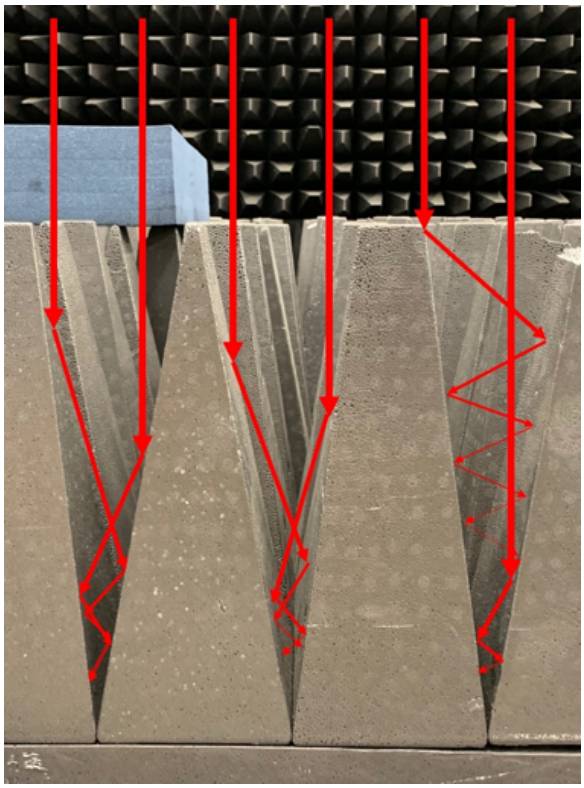

Figure 2.10: Illustration of Absorber Reflecting Wave Front

an analysis of the performance of absorber of different thicknesses being energized by waves at different incidences. It is found that as the angle of incidence increases, the reflectivity increases [14]. Also, that thicker absorber has lower reflectivity. Based on observation of these results, it is good practice to design the chamber such that the angle of incidence of a waveform not exceed 45°.

2.5 Software Defined Radio (SDR)

Software Defined Radio (SDR) is an emerging technology which allows for cheap hardware to mimic otherwise expensive components in radar systems [27]. SDRs can be programed for an extensive variety of uses. Instead of using fixed hardware components, SDRs use variable hardware controlled by software environments [10]. One such environment used is called GNU Radio. GNU Radio was first used by amateur radio operators due to it being open source and well documented [23]. The term SDR was first used by Joseph Mitola in his survey of software radios [24]. One of the first heavily funded software defined radio projects was a military program called Speakeasy [20]. In this program, the objective was to emulate existing military communications and electronic warfare (EW) platforms using SDRs due to the cost and open architecture advantages. Since Speakeasy, the reasons for continued pursuit of SDR research remain the same to this day, the ability to rapidly mimic a wide variety of RF systems, often for prototyping purposes. SDRs in conjunction with GNU Radio can be used to function as a passive radar system with a bistatic range of 35 km [15]. In [29], GNU Radio is used for the investigation of FMCW weather radar and particle motion detection. Similarly, GNU Radio and SDRs are used to investigate stationary and moving target detection in [6]. The final example mentioned here uses an SDR receiver to monitor aircraft RCS for classification [28]. These are just a few examples of this technology being pursued in the RF community.

For use in the academic environment, SDRs are fantastic to use as a learning tool as they are both cheap and capable enough to grant a hands-on introduction to RF and radar systems. For this thesis, the available SDR in the Mumma Lab is the B210

by Ettus Research. Figure 2.11 shows the SDR. The RF parameters and sampling rate of the device are sufficient to perform the operations in this thesis.

Figure 2.11: Ettus B210 SDR

Traditional antenna arrays must be physically connected by RF components due to precise phase requirements for each antenna element. Realistically, these systems cannot be built to the extreme sizes demanded by the RF community. The flexibility of SDRs makes them an ideal candidate to implement the RF backend for a digital at every element sparse array system.

CHAPTER 3

Calibration

3.1 Technique

To achieve coherence at an arbitrary target location in space using a sparse array, a typical approach using the principles discussed in the previous chapter cannot be used. This is because the direction of the target, θ and ϕ, as well precise knowledge of the distances between elements, d are unknown. For coherence, the signals from each radiating element must reach the target with the same delay in time and have the same phase. GNU Radio is capable of adjusting these two parameters for the waveforms on each channel. The values of the parameters for coherence is determined by a receiver channel. In the design problem, the transmission signals reflect off a target and onto receive elements. Greater challenges are expected with this approach and thus the environment is modified such that the receive element is in the location of the target. When multiple signals impact a target, their sum is reflected from the target with additional effects. Similarly, when multiple signals reach a receive antenna the same occurs summing effect occurs. Thus, the measurements are setup in this fashion. The next challenge is to separate each element's signals, or channel, from the summed receive waveform. This is accomplished by use of orthogonal waveforms and matched filtering. Both of these concepts will be discussed in this chapter. The

matched filter outputs for each channel produce a peak at the location of that channel in the received waveform. From here, the indices of the peaks for each channel is found as well as the phase of the signal at the peaks. The difference between the indices of the peaks and the phases gives the calibration parameters to align the channels in both time delay and phase. Figure 3.1 shows a block diagram of this system.

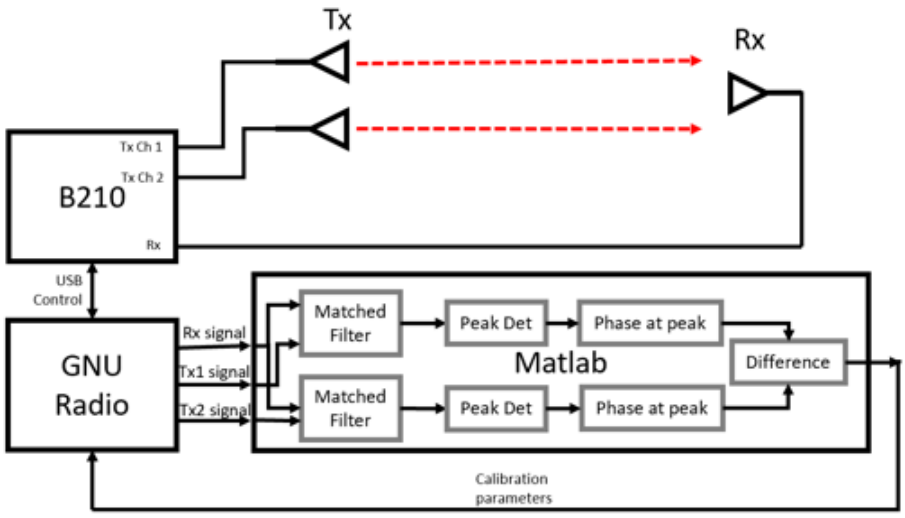

Figure 3.1: Block Diagram of Full In-situ Calibration System

3.2 Orthogonal Waveforms

In order to isolate the channels transmitted from each element contained in the received signal, the desired channel must emerge by filtering all other signals. A matched filter is employed to accomplish this due to the maximal signal to noise ratio (SNR) that matched filtering provides. However, the signals for each channel must be orthogonal in order to allow filtering of the other channels. Two orthogonal signals are considered perpendicular, as the inner product between them is zero. For the two

channel configuration in this work, the orthogonal signals chosen are linear frequency modulated (LFM) up and down chirps. The chirps are set to sweep from -2 MHz to 2 MHz and can be seen in the top left of Figure 3.2.

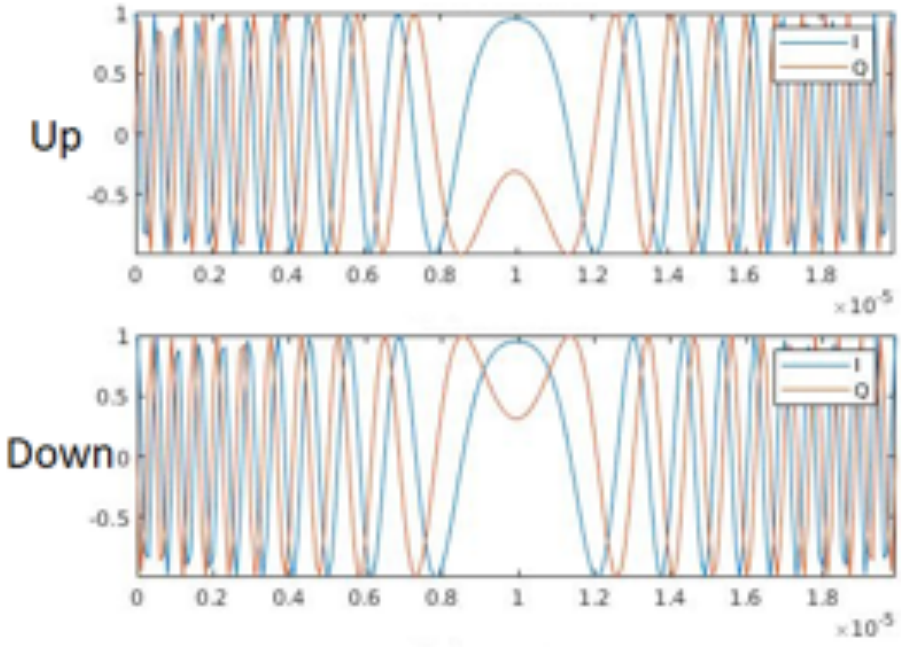

Figure 3.2: Two LFM Orthogonal Waveforms

3.3 Coherence Algorithm

To simulate the testing environment, the up and down chirps are imported into GNU Radio and transmitted from each channel on the Ettus B210 SDR. In GNU, an arbitrary delay of 400 samples is applied to the down chirp signal. The two channels are summed using a power combiner and then fed back into one of the receive ports on the USRP. The closed loop test setup can be seen in Figure 3.3. The received signal can be seen in the top left of Figure 3.4. The signal is then imported into

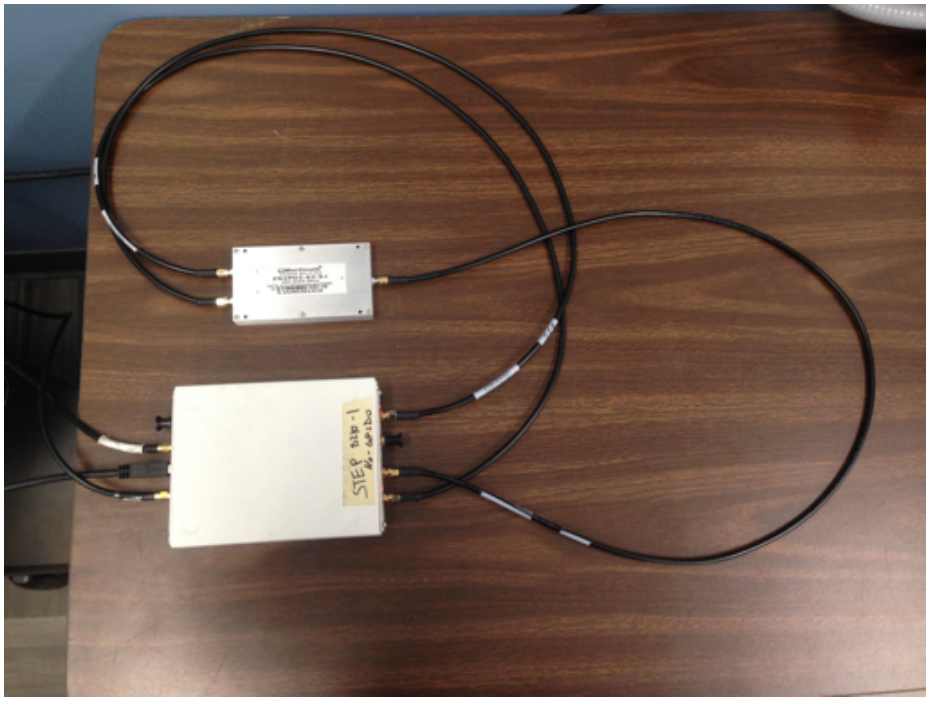

Figure 3.3: Closed Loop Test Setup Using B210 and Power Combiner

Matlab and two matched filters are applied to extract each signal. A matched filter is described by Equation 3.1.

$$y(t) = x(t) \circledast s^*(T_m - t) \tag{3.1}$$

where $x(t)$ is the received signal, $s^*(T_m - t)$ is the time reversed complex conjugate of the transmission signal $s(t)$, $y(t)$ is the output of the matched filter and T_m is the time of the peak signal output. For this setup, two matched filter outputs are required with the transmission signal from each channel represented by $s^*(T_m - t)$. To locate the position of the chirps and determine the delay in samples between channels, a peak finding algorithm is applied. The lower half of Figure 3.4 shows this result. By calculating the difference in indices at the location of the peaks for the up and down chirps, the sample delay between each channel can be calculated as well

as the determination of channel is leading and needs to be delayed. The difference

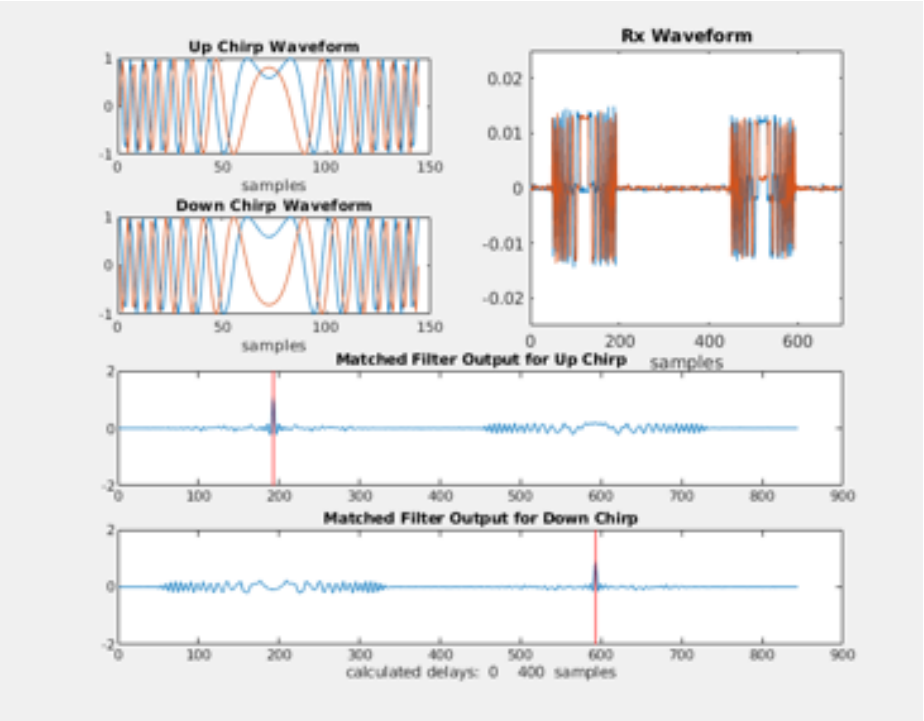

Figure 3.4: Illustration of Matched Filter Usage and Peak Finding for Orthogonal Signals

in phase is calculated by extracting the phase from the complex numbers at each of the indices found. The difference in phase between channels is then calculated in a similar manner.

However, for a radar system using pulse repetition, the time and phase delay between channels may exceed the pulse repetition interval (PRI) and the algorithm will only be able to determine the differences between nearest pulses. To solve this, rather than continuous repeated pulses, periodic gaps are inserted to exclude several pulses in a row. Figure 3.5 illustrates this. The blue signals represent the matched

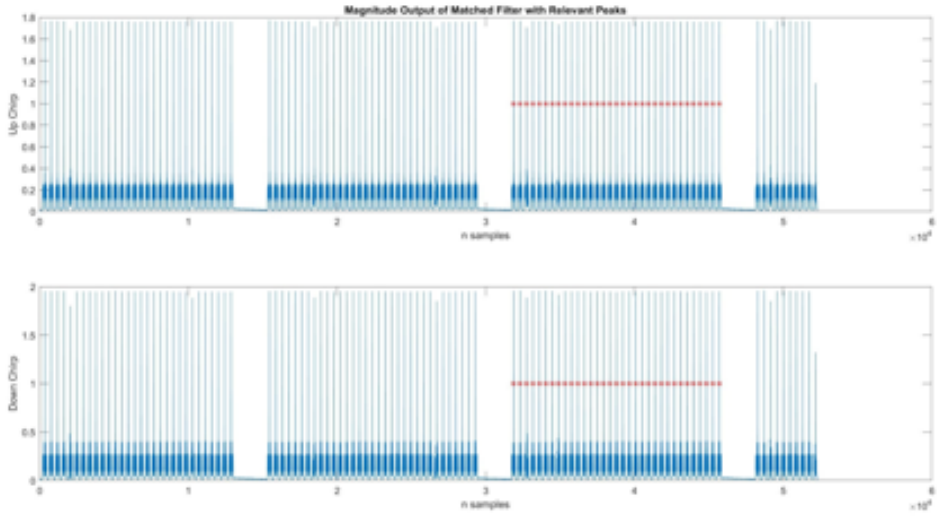

Figure 3.5: Repeated Pulse Train with Gaps for Correct Delay and Phase Difference Calculations

filter outputs of the up and down chirps respectively. A grouping of pulses separated by the inserted gaps is called a burst. Three full gaps can be seen within the capture window on both signals. After matched filtering and peak finding is performed, a set of peaks across the whole signal is created for each channel. An algorithm is then run to align the signals in time by positioning the bursts and gaps in the indices of the peak sets. It is presumed that each channel will not be delayed in time so greatly that the gaps will erroneously align with a previous or upcoming gap in the other signal. The gap alignment algorithm presumes that the second complete burst with gaps both ahead and behind the burst must align with the second complete burst on each channel. The red stars on Figure 3.5 represent the algorithm determining which peaks align on each channel. Finally, the averages of the delays in samples and phase between the red stars on each channel are used to represent the delay in

time and phase difference between each channel. These differences are compensated for in GNU Radio by use of delay blocks and complex value multiplication. Finally, the signals are retransmitted with the first set of corrections and the calibration is run again to ensure proper adjustment. Once the delay in samples reaches a value of zero and the phase difference between channels falls to less than 1°, the signals are deemed to be coherent at the receiver location. From this point, the direction of the target can be determined with general knowledge of the location of the transmission elements and the time delays used in calibration.

In a four channel configuration, the algorithm does not fundamentally change for the exception of the orthogonal waveforms. The requirement is thus present for four orthogonal waveforms. Orthogonal polyphase waveforms optimized by a novel hybrid algorithm by Hai Deng are used to satisfy this purpose [9]. These waveforms can be seen in Figure 3.6.

3.4 Stability

To test the stability of the calibration, the set up and tested again in loopback mode. Meaning the two transmission channels are fed into a power combiner which is then fed into the receive port on the B210. The algorithm still uses the up and down chirps as the orthogonal waveforms and is set to align the two channels to zero sample delay and less than 1° phase difference between channels. Once coherent to this constraint, the program continues to run for 30 minutes, measuring the phase difference between channels every 10 seconds. This procedure repeated 40 times. The first configuration utilizes the B210 with no external reference clock. The test is run and the data is projected onto a box and whiskers plot shown in Figure 3.7.

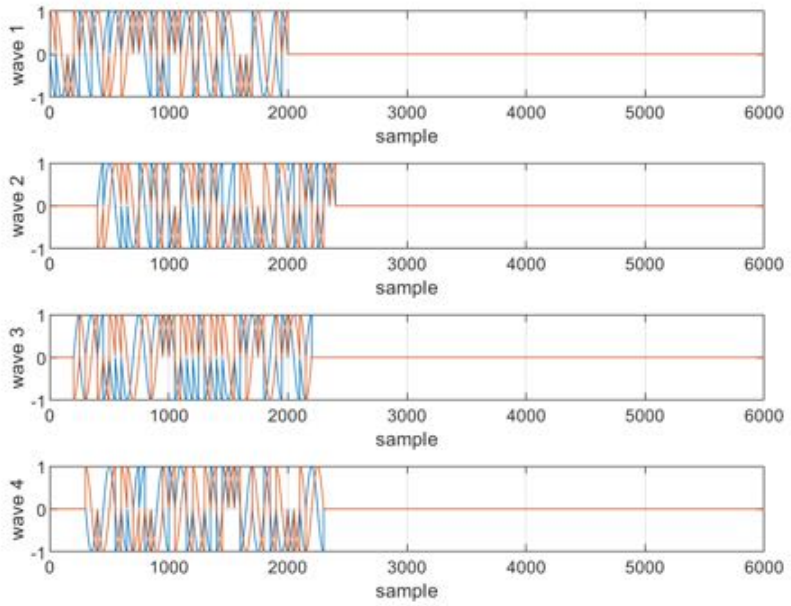

Figure 3.6: Polyphase Orthogonal Waveforms by Hai Deng

The dashed lines represent the full range of phase differences measured. The blue represents the range which contains 75% of the values and the red horizontal line is the mean. The red crosses are the outliers. At Time = 0 minutes, all the values can be seen collected at 1°. From 0 to 1 minute and 40 seconds, the phase is coherent to within 0.5°. After this however, the phase difference expands to 3° until the end of the 30 mins. There are occasional periods in which the values drop to within 0.5° however this is disregarded as the outliers still remain at the 3° level and the changes are not consistent. The test is repeated with the use of an external rubidium clock for the B210. The device used is the Stanford Research Systems (SRS) FS725 Rubidium Frequency Standard. With the frequency "Locked", the 10 MHz output is connected to the reference port on the B210 and the test is repeated. Figure 3.8. It is noted

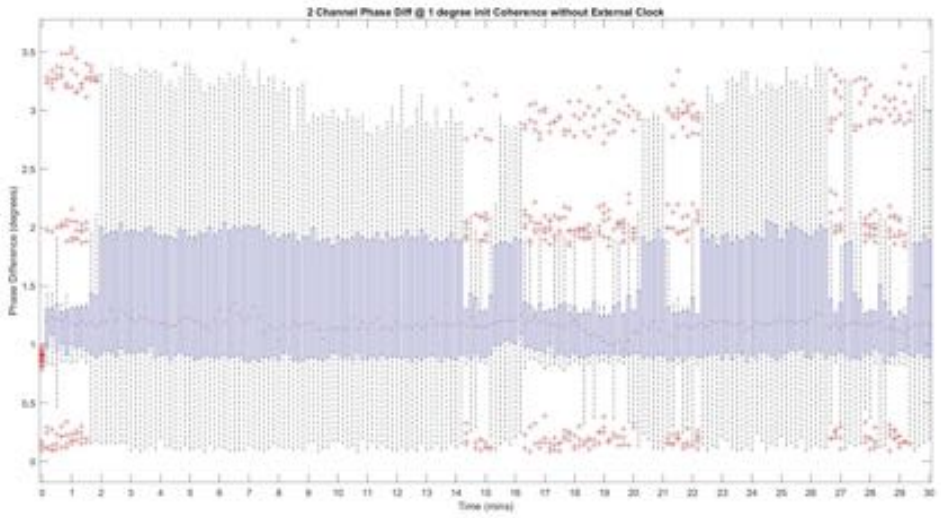

Figure 3.7: B210 Coherence Stability Test with No External Reference

that at Time = 0 minutes, more of the phase difference values approach 0° than in the test without an external reference clock. For the first minute, the phase difference expands to 2° instead of 0.5° on the last test. Similarly, throughout the remainder of the 30 mins the maximum phase difference holds at about 3°. The main difference is lack of phase difference drops and inconsistencies. All these observations take careful note of otherwise minuscule details. It is deemed that a maximum of 3° possible phase difference after 30 minutes is acceptable for the following measurements using the B210. It is also decided that the difference in results between the tests with and without the external clock, in terms of maximum phase difference observed, are not sufficient to warrant use of the clock in further tests. Thus, the measurements are taken without an external reference clock.

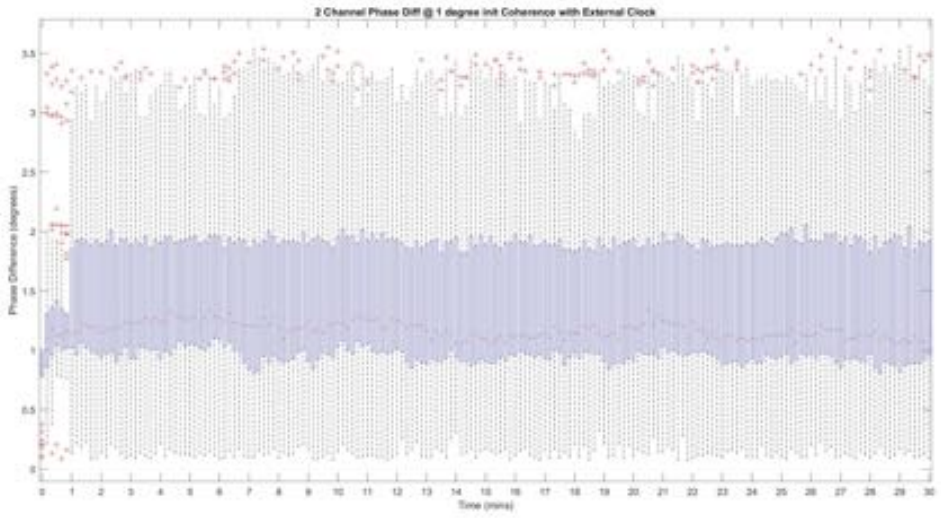

Figure 3.8: B210 Coherence Stability Test with SRS Rubidium External Reference

CHAPTER 4

Lab Measurement

4.1 Mumma Chamber Setup

In order to examine the effects of sparse arrays, several antenna configurations must be used with varying number of elements and non-uniform spacing [13]. When the spacing between antenna elements in an array exceeds $\frac{\lambda}{2}$ grating lobes start to appear [35]. At 5 GHz, $\frac{\lambda}{2} = 3cm$. Thus, to examine the effects of a sparse array, the spacing between the transmission elements must exceed this. The antennas used are the WA5VJB 850-6500 MHz Log Periodic shown in Figure 4.1. The width of the rear section of the antenna is 13.5 cm wide. In order to keep the antennas on the same plane such that they do not overlap, the spacing between the antennas cannot be less than this rear width. A spacing of 15 cm is chosen. The original mounting configuration with two antennas installed is shown in Figure 4.2. Two pieces of 1" PVC pipe were slotted allowing the antennas to be slid into place and held in by the slot. The spacing between elements could be determined by measurements drawn on the PVC pipe next to the slot. The antennas are held near the front by the slot because the SMA cable connecting to the front of the antenna put an appreciable load on the antenna and sliding the antenna forward in the slot risks breaking the antenna. However, this design was significantly improved because the PVC slot is directly contacting the

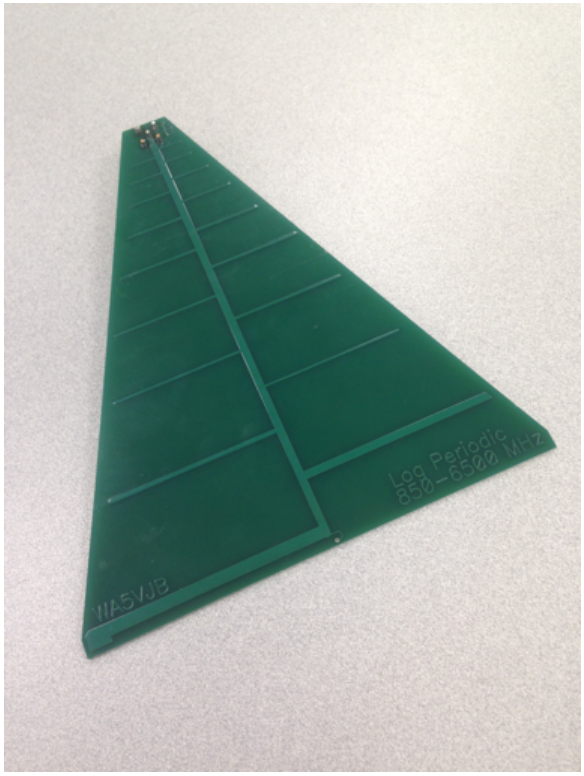

Figure 4.1: WA5VJB Log Periodic Antenna

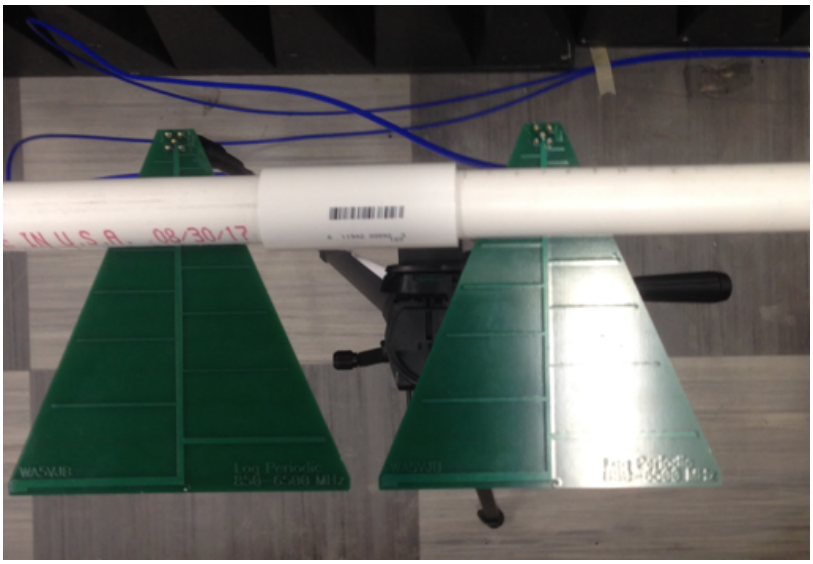

Figure 4.2: Original Mount for Two Antennas with 15 cm Spacing

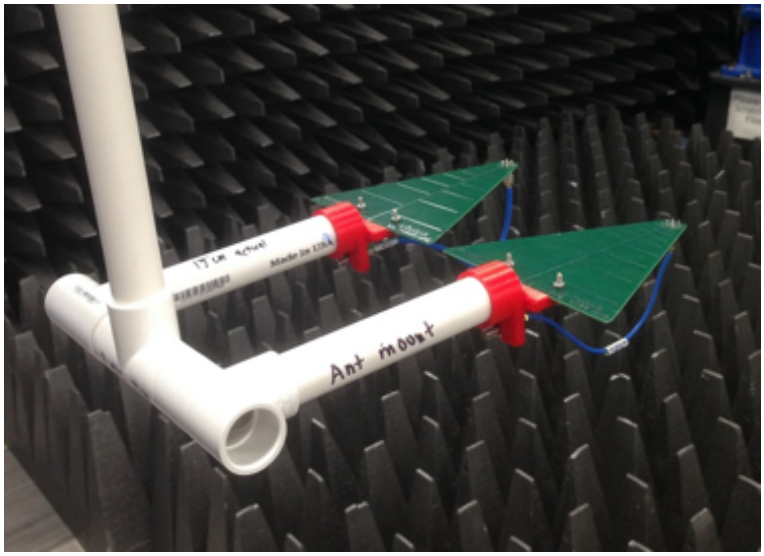

Figure 4.3: Improved Mount for Two Antennas with 15 cm Spacing

antenna near the front of the radiating element in the near field and is likely causing considerable reflection at certain frequency bands related to the lengths of conducting material on the antenna covered by the PVC. Also, it is difficult to ensure the antennas are at exactly the correct spacing and are directed in the same direction. Modification of a 3D antenna mount model found on the WA5VJB website and use of 3D printing provided by the University of Dayton Research Institute (UDRI) resulted in the construction of an improved mount. Figure 4.3 shows the antenna mount with 15 cm spacing. From the relationship between antenna aperture size and gain as well as the principles of sparse arrays, it is presumed that if the spacing between transmission elements is increased, the beam pattern obtained by the planar scan will contract toward boresight and reveal more grating lobes. A spacing of 25 cm is chosen for the second configuration and the two element array is modified to mount the antennas. Figure 4.4 shows this. Finally, a four element array is constructed where all four

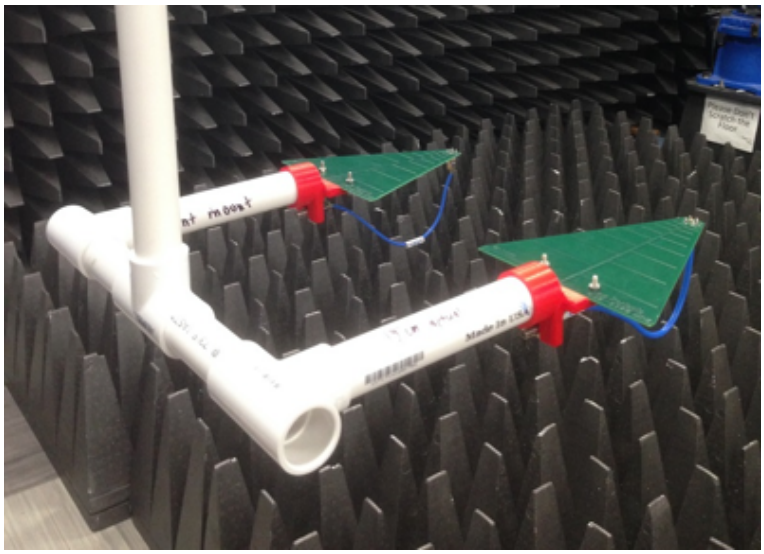

Figure 4.4: Mount for Two Antennas with 25 cm Spacing

elements are aligned in a row with 15 cm spacing between each element. Likewise, it is expected that the pattern will contract even further and show reduced grating lobes as explained in [35]. This mount is shown in Figure 4.5.

Given the semi-anechoic nature of the Mumma Lab, it is nearly impossible to obtain the true radiation pattern of an antenna or antenna array. The various reflective obstacles, non-ideal nature of the absorber and range of motion of the robots restrict the types of scans to perform. The chamber in the Mumma Lab can be seen on Figure 4.9 with the measurement equipment set up.

Due to the available range of motion of the robots and the method of data capture, it is decided to perform planar scans. Meaning, the receive element near the back in Figure 4.9 moves in the up/down, left/right plane from the viewer's perspective of the picture. The transmission elements do not move, as it is the objective of the receive element to capture a 2D scan of the radiation pattern of the transmission element

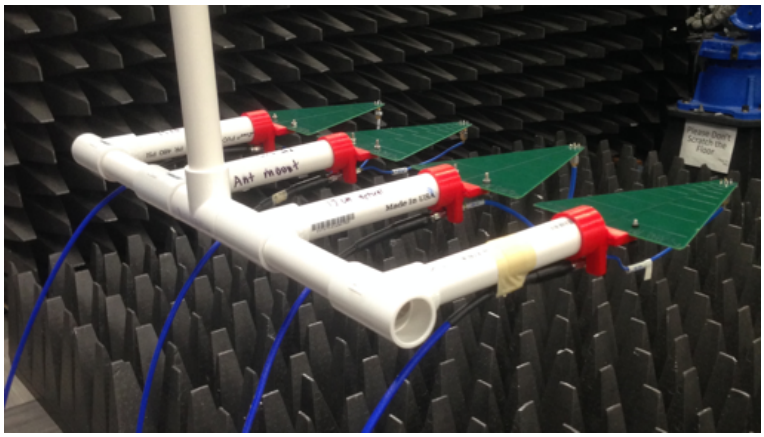

Figure 4.5: Mount for Four Antennas with 15 cm Spacing

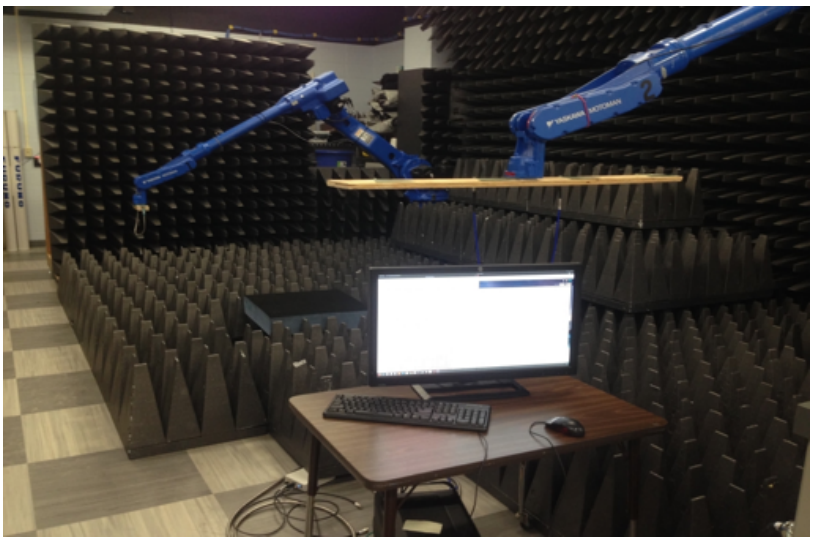

Figure 4.6: Test Configuration 1 Semi-Anechoic Chamber in the Mumma Lab

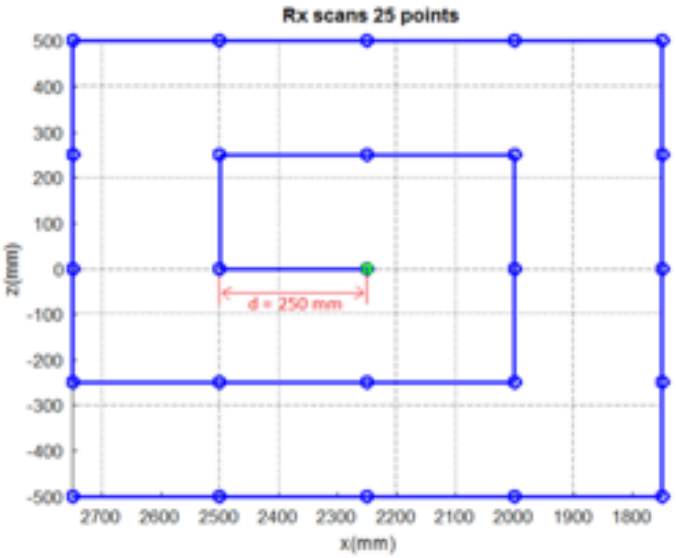

Figure 4.7: 25 point Spiral Pattern Diagram

at several locations on the plane. The receive element is moved to the locations in the plane in a spiral pattern. An illustration of the movement pattern can be seen in Figure 4.7. At each point on the blue path, the robot pauses at that location and performs a data capture between the transmission elements and the receive element. The power is measured at each point and is plotted. To obtain an image of the data with sufficient resolution, the number of points in the spiral pattern is increased to 1089 by scanning a plane of 33 by 33 points. The next decision is the orientation of the elements in the chamber during measurement and the exact size of the plane. The first consideration is that the receive element must not be within the near field of the transmission array. Using the far field approximation defined by 2.2, at 5 GHz and effective aperture sizes of 15 cm and 25 cm for the two element arrays, the far field is calculated to start at a radial distance of 0.75 m and 2.1 m respectively from boresight of the array. To satisfy this, the distance between the transmission array

and center of the receive scan plane is set to 3 m. For the four element array, with an effective aperture of 45 cm, the far field starts at 6.75 m. There is no dimension in the Mumma chamber which can accommodate this radial distance. Thus, the four channel data will be captured in the near field.

As for the area of the plane, it is desired that the scans have a range of at least $\pm 10^{\circ}$ in both azimuth and elevation. Given the range of motion of the robot holding the receive element and the 3 m distance between the transmission array and receive element, a square plane of $\sim 1m^2$ is chosen. A more specific value is chosen after the following test.

4.2 Test Measurements

The challenge of performing tests in a semi-anechoic chamber is determining how the radiated energy will interact with non-anechoic artifacts in the chamber. In Figure 4.9 while there is absorber material present behind the receive element and below, the stacked absorber material to the right would reflect an appreciable amount of energy from the transmission array toward the receive element, giving incorrect measurements of the radiation pattern during the scan. Nevertheless, as a benchmark a data capture is performed with the chamber in this configuration. The transmission array is configured with 2 elements having 15 cm spacing between elements. The transmission array and receive element are distanced 3 m apart with a planar scan area is $1m^2$. The data is captured using LFM pulses generated by the Ettus B210 SDR. The two waveforms are first made coherent to the center of the scan plane by used of the calibration procedure. The data is then captured in a spiral pattern. Figure 4.8 shows the magnitude and phase data captured in the scan. It is important

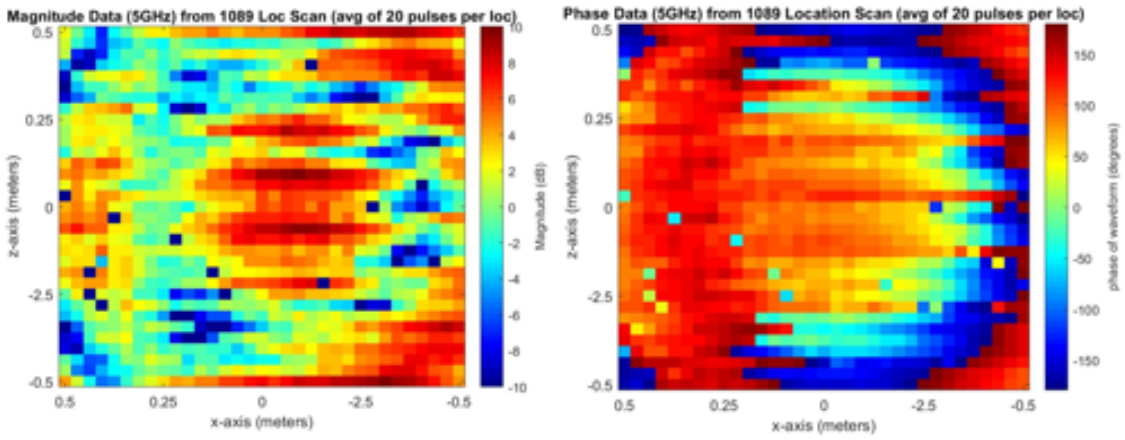

Figure 4.8: Magnitude and Phase Planar Scans in Chamber Configuration 1 with 15 cm Spacing at 5 GHz

to note that the data is captured showing instantaneous phase. This is a result of taking the complex data points data from the Fourier domain peaks of the LFM chirps. The data in the results section is plotted using signal power rather than this method. The interference seen would not be present in an ideal measurement environment. Thus, potential sources of interference in the lab are adjusted. Figure 4.9 shows an improved chamber configuration. A virtual reconstruction of configurations 1 and 2 are shown in Figure 4.10. The absorber material is rearranged and smaller pieces of absorber are added to various places where high reflectivity is expected, such as on the metallic robot arms. Also, the computer used to capture data and control the B210 is moved back away from the transmission array. The same data capture is performed in this location and the magnitude and phase data is shown in Figure 4.11. The image is much clearer however a large artifact is present on the left side of the scanned data. It is speculated that the cause of this error is the exposed concrete wall on the left side of the chamber. Figure 4.12 shows a picture of this side of the chamber. To avoid

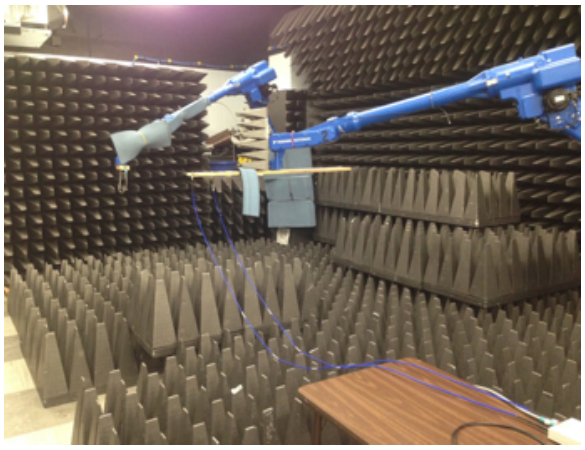

Figure 4.9: Test Configuration 2 of the Semi-Anechoic Chamber in the Mumma Lab

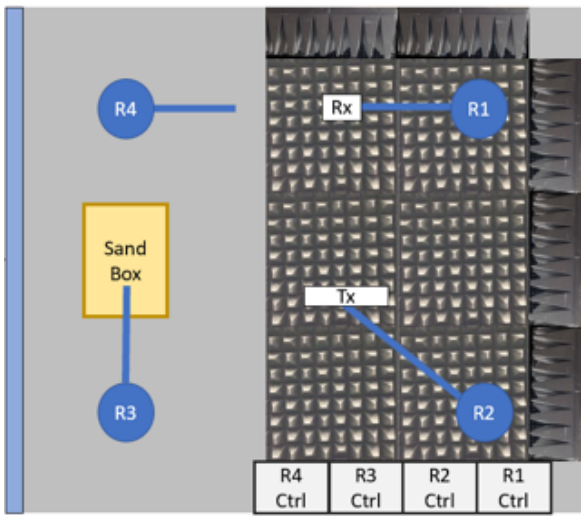

Figure 4.10: Diagram of Mumma Lab in Configuration 1 and 2

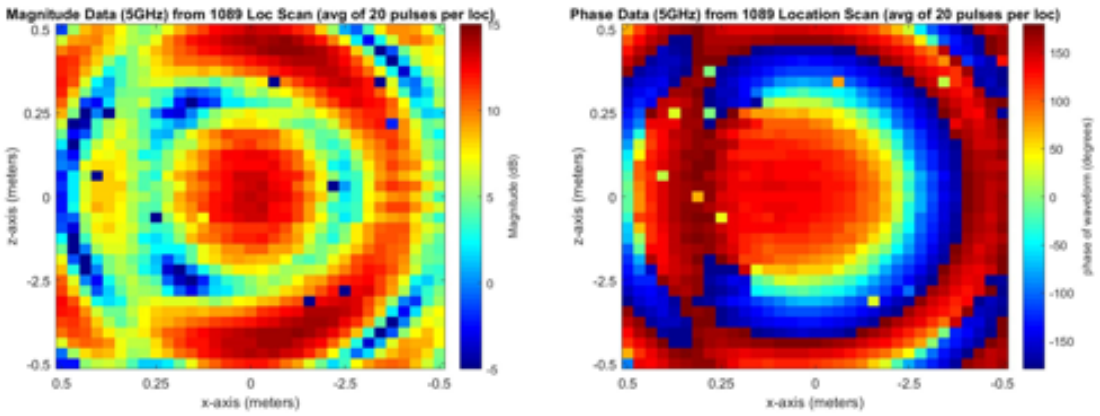

Figure 4.11: Magnitude and Phase Planar Scans in Chamber Configuration 2 with 15 cm Spacing at 5 GHz

Figure 4.12: Possible Cause of Interference in Configurations 1 and 2

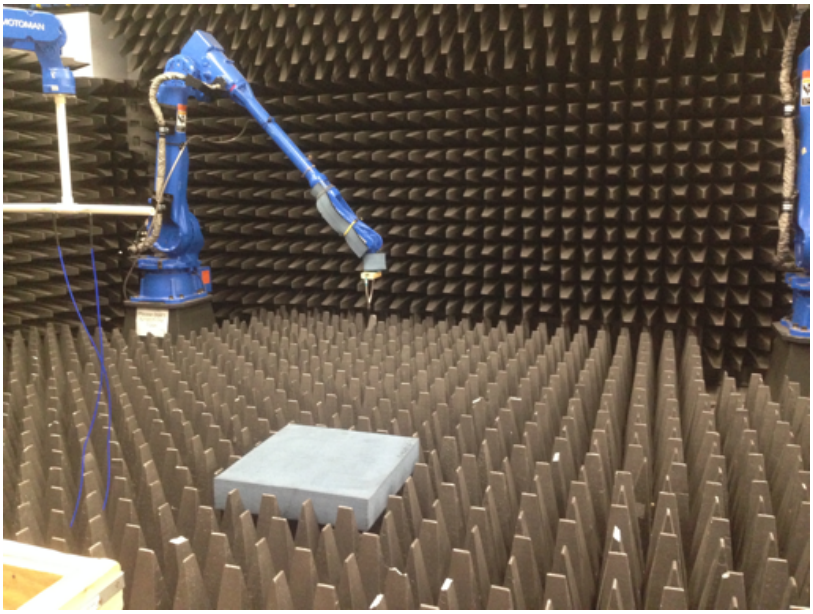

Figure 4.13: Test Configuration 3 of the Semi-Anechoic Chamber in the Mumma Lab

this problem, the entire setup is rotated to the right side of the chamber as shown in Figure 4.13. A virtual reconstruction of this configuration is shown in Figure 4.14. The same data capture is performed in this configuration and the results are shown in Figure 4.15. This image is much clearer, showing the instantaneous phase data for a planar scan of a two element log periodic array. Thus, configuration 3 is chosen for all following planar scans as it offers the minimal interference in the semi-anechoic chamber.

Next the planar scan area is defined precisely to be $1.25m^2$. This coincides with the robot's range of motion in this configuration and has an angular scan range of 11.77°. This is calculated by taking the inverse tangent of the distance from the center to the edge which is 0.625 m over the distance between the transmission array and receive element which is 3 m. The final chamber measurement configuration is

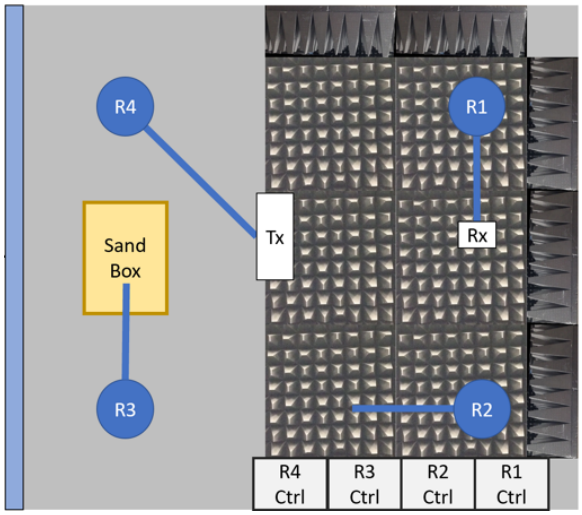

Figure 4.14: Diagram of Mumma Lab in the Configuration 3

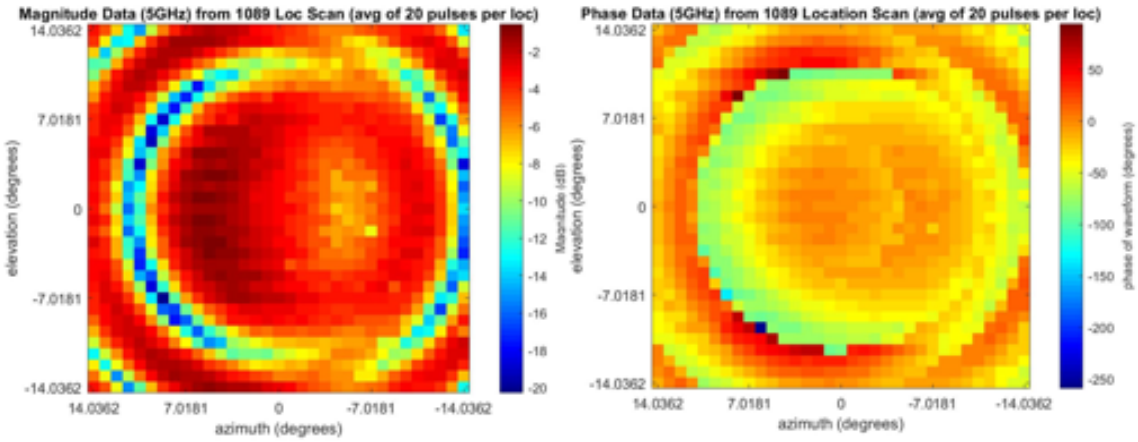

Figure 4.15: Magnitude and Phase Planar Scans in Chamber Configuration 3 with 15 cm Spacing at 5 GHz

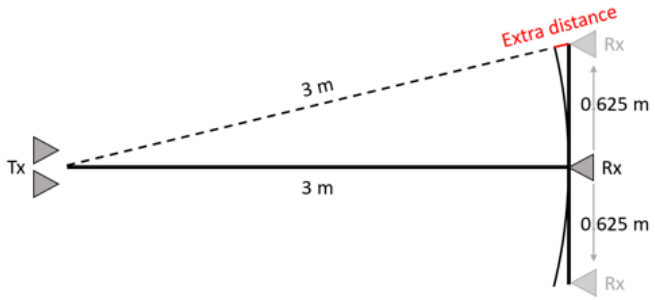

Figure 4.16: Radial Distance Error between Tx and Rx during Planar Scan

decided based on far field restrictions, interference in the semi-anechoic chamber, the range of motion of the robots and the desired dimensions of the planar scan image.

It should be noted that the radial distance between the transmission array and the receive element changes with respect to the position of the receive element on the plane. This is illustrated in Figure 4.16. The red line segment represents the extra distance the transmitted wave must travel before being received. In part, this represents the objective of the calibration. If the waves are made coherent at the center of the plane, less total gain can be expected at the edges because the waves are no longer traveling the same distance. The red line segment is 6.44 cm long. The frequency of operation, 5 GHz, has a wavelength of 6 cm. This extra distance allows the wave to perform an entire cycle before being received compared to waves received at the center of the plane. This effect is observed in both simulation and in the chamber.

4.3 Planar Scans

The following section contains all relevant recorded data in the semi-anechoic chamber in the Mumma Lab. First, a planar scan of two log periodic antennas with

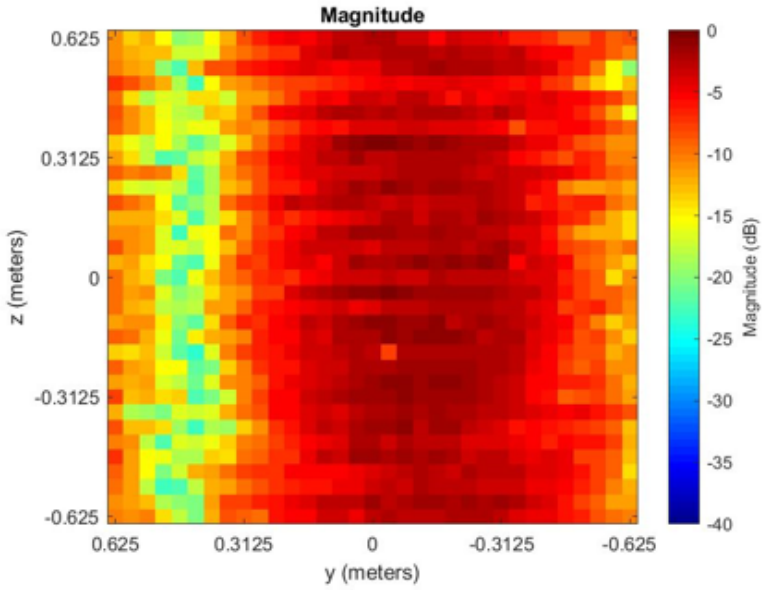

Figure 4.17: Planar scan of a two Log Periodic Antennas separated by 15 cm

15 cm separation between transmission elements is performed. The transmission and receive waveform used to gather data is a 5 GHz sinusoidal wave where the power of the signal present within the capture window is used to determine the gain at each location in the scan. It is important to note that prior to the scan, the signals of each transmission element are coherently calibrated to within 3 degrees of phase difference at the center of the scan plane. The results are shown on Figure 4.17. Then, the separation between the two antennas is changed to 25 cm and the scan is performed again. The signals are again calibrated at the start of the scan to ensure coherence. Figure 4.18 shows this result. Unfortunately, due to time and technological constraints, the four channel measurement was not performed.

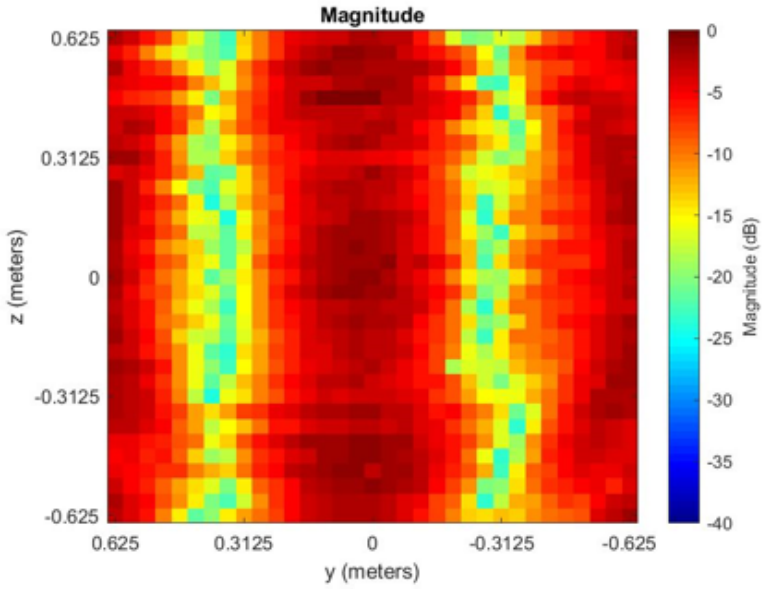

Figure 4.18: Planar scan of a two Log Periodic Antennas separated by 25 cm

CHAPTER 5

Simulation

5.1 Background

Given the advancement of modern-day computing, antennas can be modeled and measured in a virtual environment. Programs such as FEKO, HFSS and CST are a few examples of currently available simulation software. Altair FEKO is a comprehensive computation electromagnetic code provided in the MUMMA Lab at the University of Dayton. It can provide the near and far field radiation patterns in 2D or 3D for any modeled antenna.

The objective is to view the radiation pattern of a two element log periodic array in a semi-anechoic chamber using a Software Defined Radio (SDR). Due to the chamber not being fully anechoic, there are several contributions to antenna pattern interference. Thus, it is difficult to determine errors in pattern measurement or SDR performance based on the obtained results. To obtain the radiation pattern, the antenna setup is constructed in FEKO and the simulation results can be gathered. From these results, objects or conditions in the semi-anechoic chamber which cause interference can be identified.

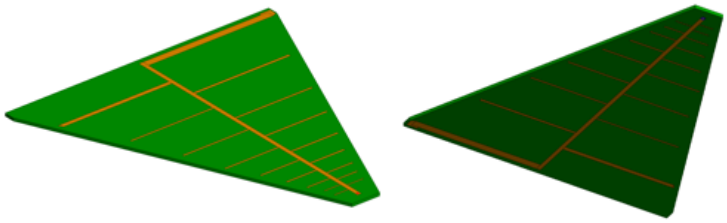

Figure 5.1: WA5VJB Log Periodic Antenna Modeled in FEKO

5.2 3D FEKO Patterns

To test this, the radiation pattern of a log periodic array will be measured in the lab and then compared to the FEKO simulation. First the log periodic antenna is modeled in FEKO. The antennas used are the WA5VJB 850-6500 MHz Log Periodic shown in Figure 4.1. The antenna is modeled in FEKO by constructing each element of the log periodic array based on physical measurement. Figure 5.1 shows the model. Note that the underside of the antenna is also in a log periodic configuration using the same measurements as the top side. A mesh is then created for the model, validation is performed, and the model is then solved. This is the typical routine for generating results from a FEKO model. The results are then opened in POSTFEKO. For a single log periodic antenna, the simulated 3D radiation pattern is shown in Figure 5.2. The ϕ and θ 2D cuts are also obtained and shown in Figure 5.3. This matches the expected pattern for the WA5VJB Log periodic antenna, thus providing substantial validation that the model was correctly constructed.

The log periodic model is duplicated so a two element log periodic array is present. The elements are separated by 15 cm on the y axis while being held the same on the x and z axes. Figure 5.4 shows this array modeled in FEKO. The model is

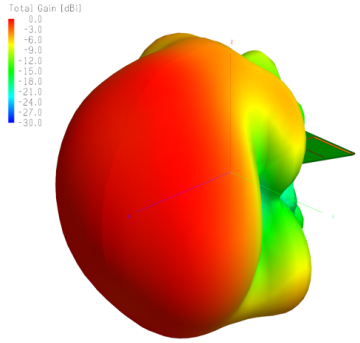

Figure 5.2: WA5VJB Log Periodic Antenna 3D Pattern Simulation in FEKO

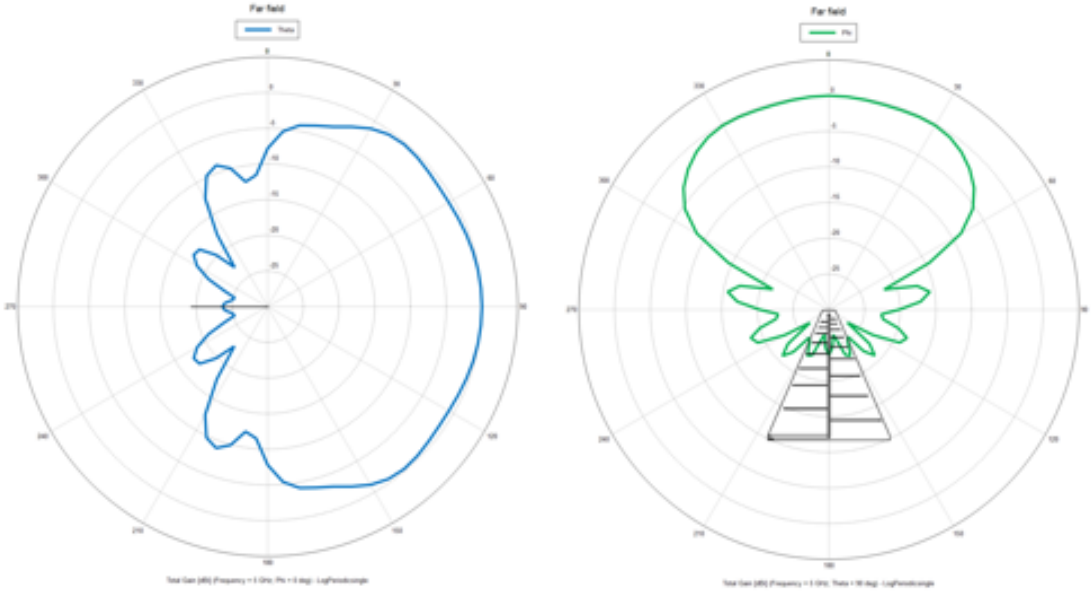

Figure 5.3: WA5VJB Log Periodic Antenna Simulated ϕ and θ cuts

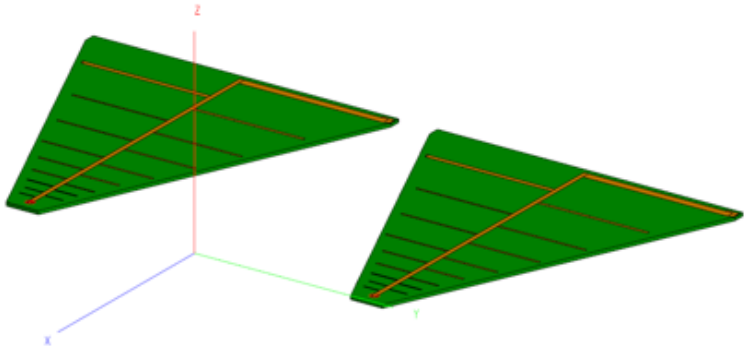

Figure 5.4: Two Element WA5VJB Log Periodic Antenna Array in FEKO

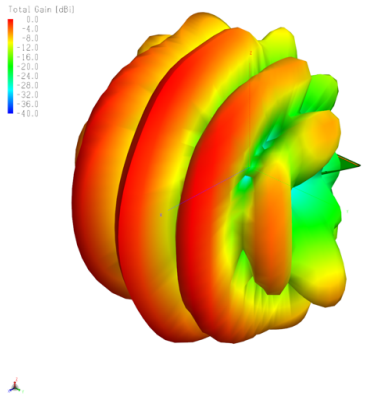

Figure 5.5: Two Element WA5VJB Log Periodic Antenna Array 3D Pattern Simulation

meshed, validated and solved again in order to generate the POSTFEKO results. The simulated 3D radiation pattern for the two element array is shown in Figure 5.5. The ϕ and θ 2D cuts are also obtained and shown in Figure 5.6. The elevation pattern is to be expected because the array is not spatially diverse in the x or z axis. The azimuth pattern however, functions in accordance with a typical array factor pattern.

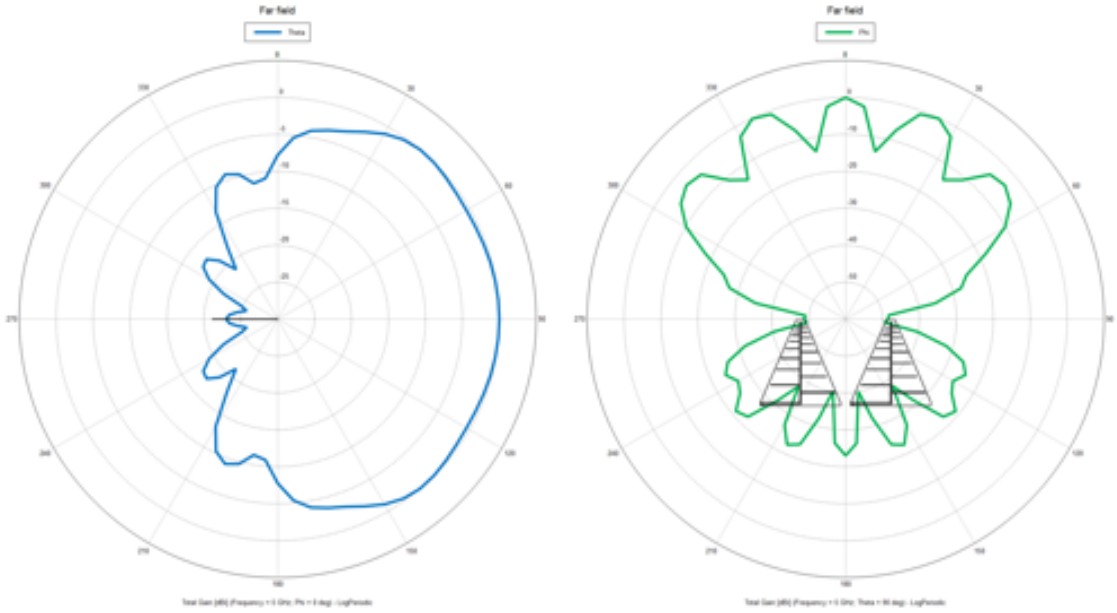

Figure 5.6: Two Element WA5VJB Log Periodic Antenna Array Simulated ϕ and θ cuts

Next, the four element array is constructed by again duplicating the array. The spacing between each antenna element is set to 15 cm and an image of the array can be seen in Figure 5.7. The model is meshed, validated and solved again in order to generate the POSTFEKO results. The simulated 3D radiation pattern for the four element array is shown in Figure 5.8. The ϕ and θ 2D cuts are also obtained and shown in Figure 5.9.

The measurements possible in FEKO are far greater than the clarity and capability of the Mumma lab. Capturing 3D patterns of the antenna arrays is not practical due to the unideal electromagnetic conditions of the chamber, the rage of motion of the robots and the configuration of the USRP program. However, it is possible to perform planar scans.

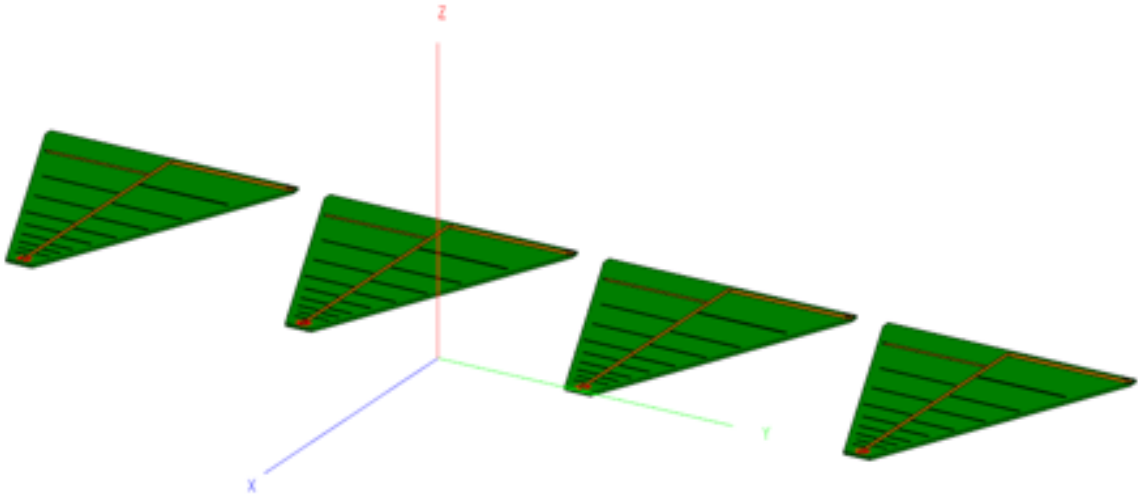

Figure 5.7: Four Element WA5VJB Log Periodic Antenna Array in FEKO

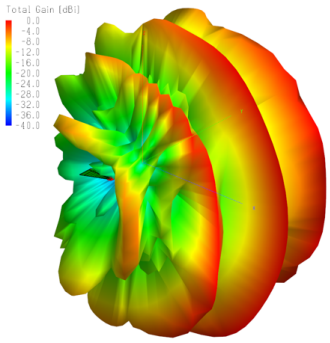

Figure 5.8: Four Element WA5VJB Log Periodic Antenna Array 3D Pattern Simulation

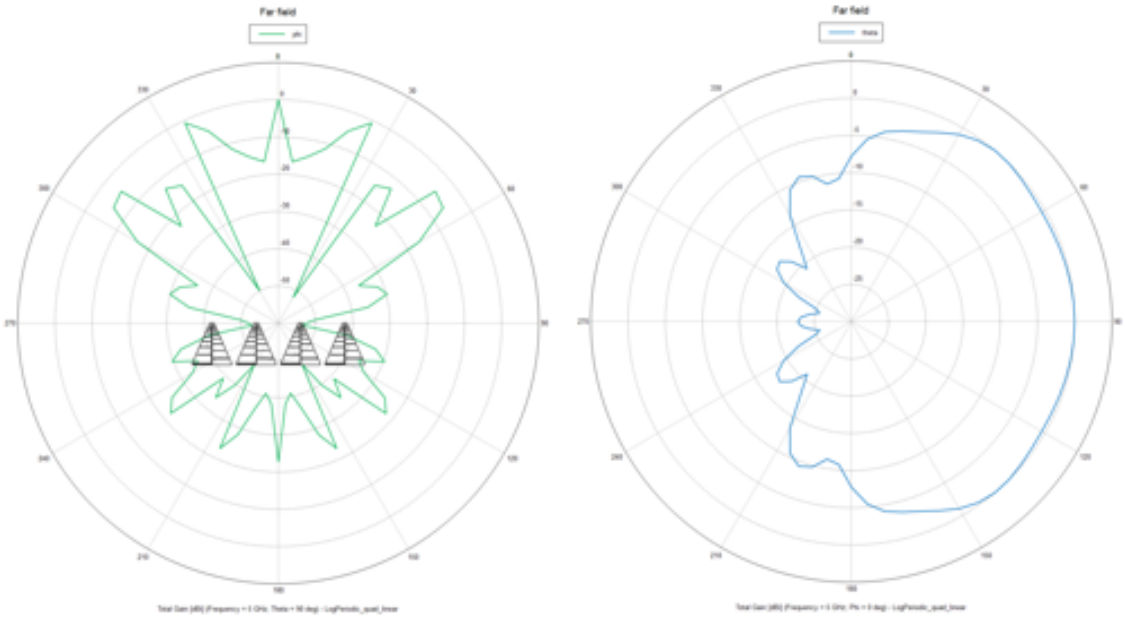

Figure 5.9: Four Element WA5VJB Log Periodic Antenna Array Simulated ϕ and θ cuts

5.3 Planar Simulation Results

In FEKO, a plane is created by measuring a 2D near field volume. The plane is positioned virtually 3 m from the antenna array with an area of 1.25 m^2. Figure 5.10 shows the position of the plane in 3D space.

Two log periodic antennas, with phase centers separated by 15 cm, are arranged in the chamber and a planar scan is recorded. The results are shown on Figure 5.11.

Then, the separation between the two antennas is changed to 25 cm and the scan is captured again. Figure 5.12 shows this result.

To complete the sinusoidal scans, two more antennas are added to the virtual environment to form a four element linear array with 15 cm separations between each element. Figure 5.13 shows this result.

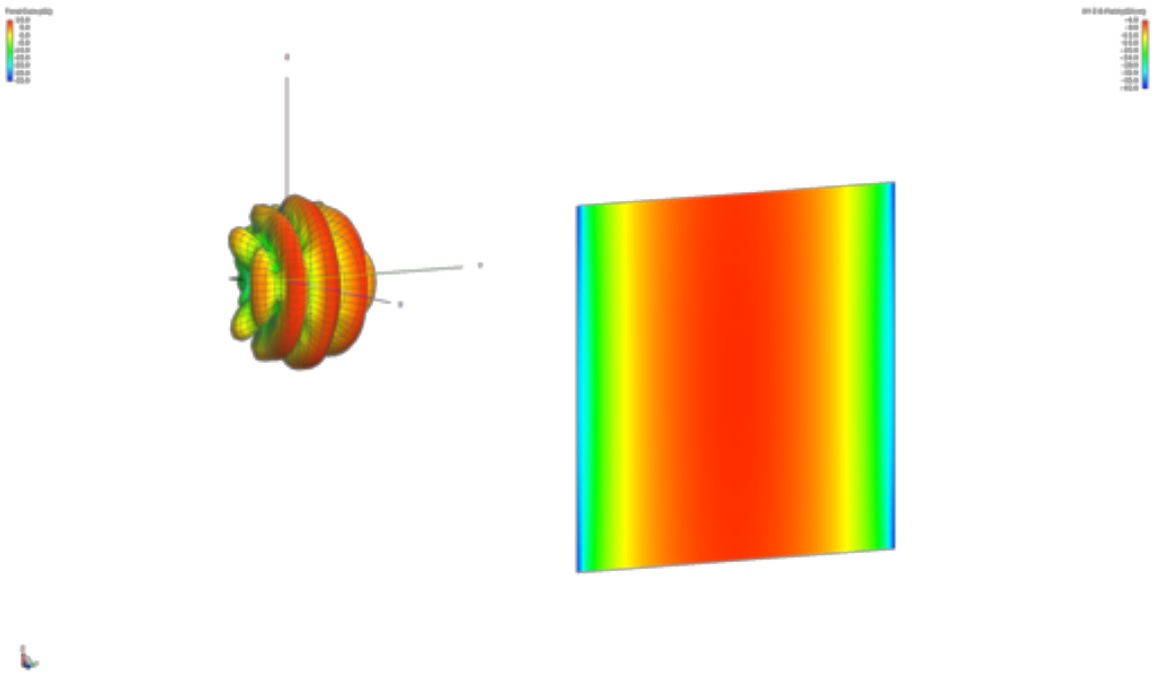

Figure 5.10: 2D plane in 3D FEKO Environment

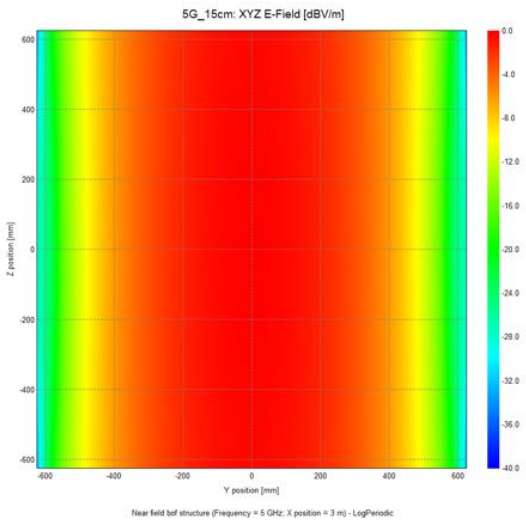

Figure 5.11: FEKO Planar scan of a two Log Periodic Antennas separated by 15 cm

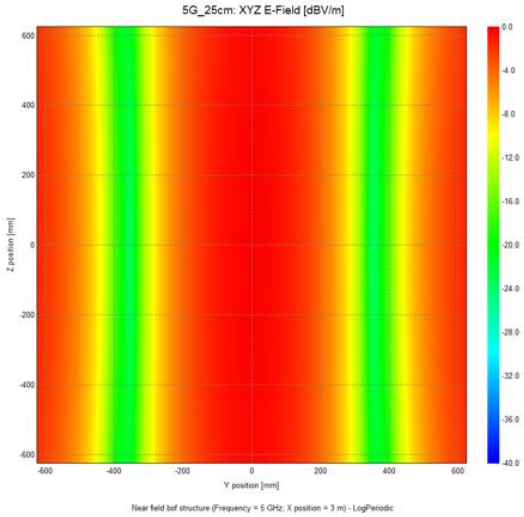

Figure 5.12: FEKO Planar scan of a two Log Periodic Antennas separated by 25 cm

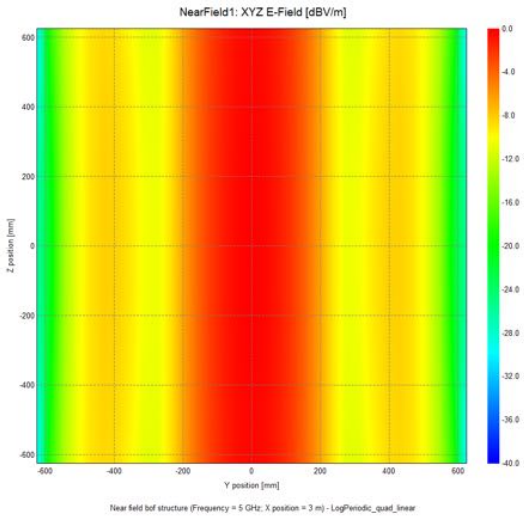

Figure 5.13: FEKO Planar scan of a four Log Periodic Antennas separated by 15 cm)

CHAPTER 6

Results

A direct comparison to the planar scan results obtained in the chamber to the results obtained in FEKO allow for better interpretation of the data. Figure 6.1 shows the measured and simulated results of the two log periodic antennas with 15 cm spacing. Initial observation shows that both images contain a wide main lobe

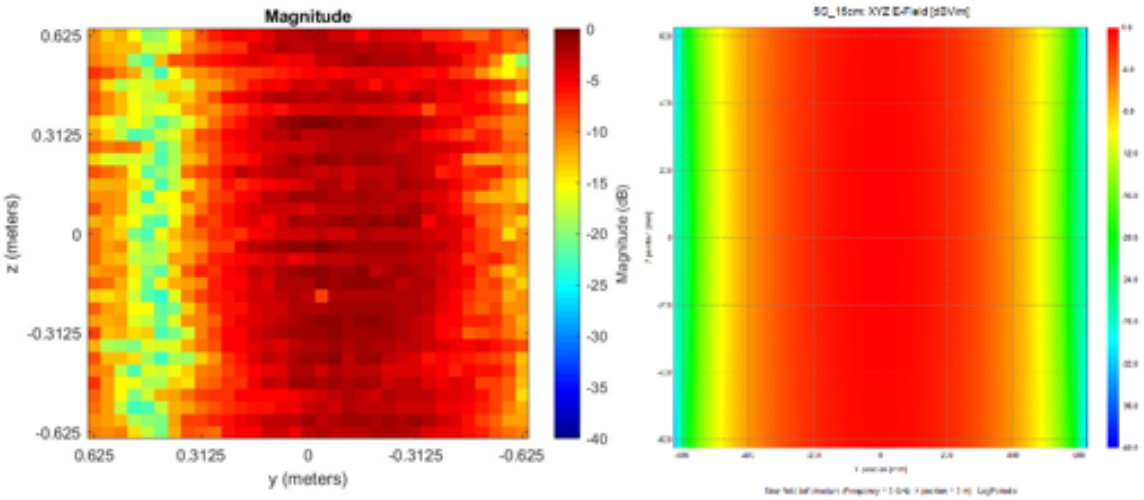

Figure 6.1: Comparison of Two Log Periodic Antennas separated by 15 cm

with nulls on the right and left. The null on the right side of the measured image is not entirely visible but it can partially be seen. It is likely that the measured

image appears shifted to the right because either the Tx and Rx elements were not aligned properly or that the coherence between the two signals was not sufficient. The positions of the nulls on the image are the same with the left and right nulls on the measured image being approximately -450 and 750 respectively, meaning they are separated by 1200 mm. The simulated shows the nulls at around -600 and 600 giving a separation of 1200 mm. Thus the nulls are approximately identical. Another observation of importance is the gain on each image. The gains on both images are calibrated to the center of the image. The half-power beamwidth appears the same for both images being around -300 mm and 300 mm from the center of the beam. The power level of the nulls differ slightly in that the measured has a minimum gain of around -25 dB whereas the simulated appears to reach -32 dB before reaching the edge of the image. Whether the minimum gain reaches lower than this value is not found. It is likely that the extra gain is introduced into the measured image as a result of measurement in a semi anechoic environment.

Figure 6.1 shows the measured and simulated results of the two log periodic antennas with 25 cm spacing. At first glance, these images bear striking resemblance despite being captured in very different environments. Both images contain the expected nulls and grating lobes within the confines of the image. The position of the nulls in the measured image are -450 mm and 300 mm respectively, giving a separation of 750 mm. The nulls on the simulated image are located at -360 and 360, giving a separation of 720 mm. Based on these approximate results it is fair to say that the images represent the same phenomenon. The half-power beamwidth shows similar values for both images as well as null gain. The nulls on the measured image appear no lower than -25 dB while the simulated image shows no lower than -24 dB.

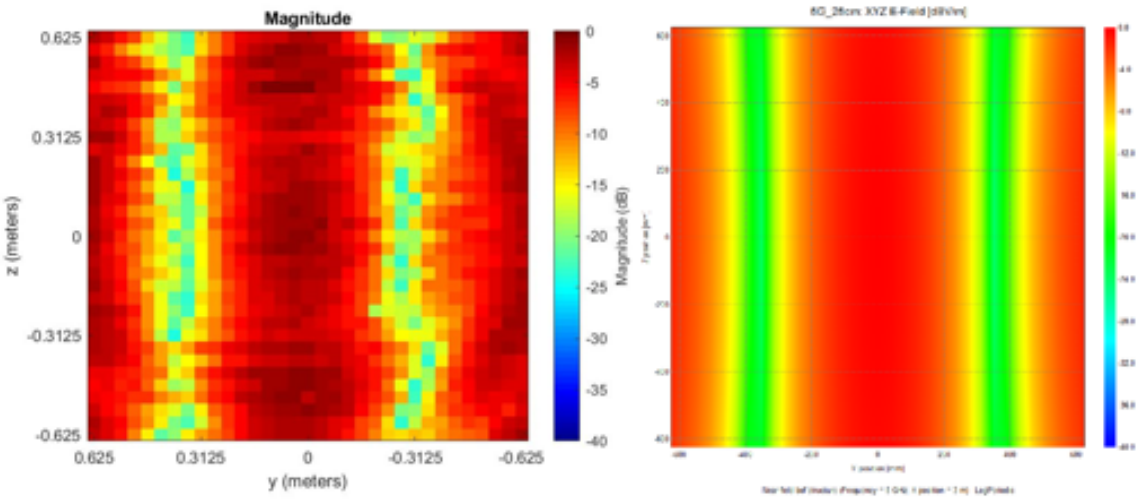

Figure 6.2: Comparison of Two Log Periodic Antennas separated by 25 cm

It is noted that the measured image contains lateral variation in the nulls, especially near the top and bottom of the image. This effect is likely another interference artifact in the chamber

CHAPTER 7

Conclusions

In this thesis, an in-situ calibration technique for arbitrarily sparse arrays is developed, measurement techniques are used in a non-ideal semi-anechoic chamber, and the experimental results are validated against industry standard electromagnetic modeling and simulation tools. It is found that despite the non-anechoic environment, similar results are obtained with matching beam patterns and magnitudes. The results also demonstrate the ability to use an SDR for data capture in a laboratory environment with acceptable results.

CHAPTER 8

Future Work

Further pursuit of the work in this thesis would involve obtaining the four channel measurement in the chamber using either a pair of B210s or the N310 USRP which features four Tx/Rx ports instead of the two that the B210 offers. The N310 also has advanced performance capabilities including a higher sampling rate and better clock stability. However, pursuit of using two B210s would involve adding a frequency matching stage to the calibration, due to the error in clock speed between two B210s. a difference in clock speed means the transmitted waves, while set to output the same frequency would differ by the clock speed error. This was not a problem when using one B210 because both waveforms transmitted experienced the same clock error and thus did not differ in frequency when set identical. The solution to frequency matching two B210s was idealized but never tested due to time constraints.

Another further development would be altering the chamber setup such that the Tx signal would reflect off a target and be received by another set of antennas. This setup would further encompass the problem of cohering to a target based on the reflected signal which is bypassed in this thesis by placing an Rx antenna at the target location. Building this reflecting target setup would present more challenges

and allow for further discovery of problems which could be addressed to improve the coherence algorithm and sparse antenna setup.

BIBLIOGRAPHY

[1] Ieee standards test procedure for antennas. *IEEE Std 149-1955 (ANSI C16.11-1971)*, pages 1–29, Jan 1965.

[2] Abm research and development at bell laboratories: Project history. Technical report, October 1975.

[3] Ieee standard test procedures for antennas. *149-1979: IEEE Standard Test Procedures for Antennas*, page 01, 1979.

[4] Mimo radar: an idea whose time has come. *Proceedings of the 2004 IEEE Radar Conference (IEEE Cat. No.04CH37509), Radar Conference, 2004. Proceedings of the IEEE, Radar conference*, page 71, 2004.

[5] Onery range brochure. `https://www.wpafb.af.mil/Portals/60/documents/T2/20171004%20OneRY%20Range%20Brochure%2088ABW-2017-1943.pdf`, 2017. Accessed: 2019-02-11.

[6] S. Aulia, A. B. Suksmono, and A. Munir. Stationary and moving targets detection on fmcw radar using gnu radio-based software defined radio. In *2015 International Symposium on Intelligent Signal Processing and Communication Systems (ISPACS)*, pages 468–473, Nov 2015.

[7] C. A. Balanis. Antenna technology: Past, present and future. In *2012 IEEE International Workshop on Antenna Technology (iWAT)*, pages 5–7, March 2012.

[8] Constantine A Balanis. *Antenna theory: analysis and design*. Wiley-Interscience, 2005.

[9] Hai Deng. Polyphase code design for orthogonal netted radar systems. *IEEE Transactions on Signal Processing*, 52(11):3126–3135, Nov 2004.

[10] Markus Dillinger, Kambiz Madani, and Nancy Alonistioti. *Software defined radio. [electronic resource] : architectures, systems, and functions.* Wiley series in software radio. Hoboken, NJ : Wiley, c2003, 2003.

[11] W. Emerson. Electromagnetic wave absorbers and anechoic chambers through the years. *IEEE Transactions on Antennas and Propagation*, 21(4):484–490, July 1973.

[12] A. M. Haimovich, R. S. Blum, and L. J. Cimini. Mimo radar with widely separated antennas. *IEEE Signal Processing Magazine*, 25(1):116–129, 2008.

[13] M. B. Hawes, W. Liu, and R. J. Langley. Sparse antenna array design via compressive sensing. In *IET Colloquium on Antennas, Wireless and Electromagnetics 2014*, pages 1–17, May 2014.

[14] Leland Hemming. *Electromagnetic anechoic chambers : a fundamental design and specification guide*. IEEE Press Wiley Interscience, Piscataway, NJ New York, 2002.

[15] S. Heunis, Y. Paichard, and M. Inggs. Passive radar using a software-defined radio platform and opensource software tools. In *2011 IEEE RadarCon (RADAR)*, pages 879–884, May 2011.

[16] C. L. Holloway, R. R. DeLyser, R. F. German, P. McKenna, and M. Kanda. Comparison of electromagnetic absorber used in anechoic and semi-anechoic chambers for emissions and immunity testing of digital devices. *IEEE Transactions on Electromagnetic Compatibility*, 39(1):33–47, Feb 1997.

[17] H. A. Khan, W. Q. Malik, D. J. Edwards, and C. J. Stevens. Ultra wideband multiple-input multiple-output radar. In *IEEE International Radar Conference, 2005.*, pages 900–904, May 2005.

[18] John W. Klooster. *Icons of invention : the makers of the modern world from Gutenberg to Gates.* Greenwood icons. Santa Barbara, Calif. : Greenwood Press, c2009., 2009.

[19] D. G. Kurup, M. Himdi, and A. Rydberg. Synthesis of uniform amplitude unequally spaced antenna arrays using the differential evolution algorithm. *IEEE Transactions on Antennas and Propagation*, 51(9):2210–2217, Sept 2003.

[20] R. I. Lackey and D. W. Upmal. Speakeasy: the military software radio. *IEEE Communications Magazine*, 33(5):56–61, May 1995.

[21] J. Li and P. Stoica. Mimo radar with colocated antennas. *IEEE Signal Processing Magazine*, 24(5):106–114, Sep. 2007.

[22] Lianlin Li, wenji zhang, and Fang Li. The design of sparse antenna array. 2008.

[23] R. G. Machado and A. M. Wyglinski. Software-defined radio: Bridging the analog–digital divide. *Proceedings of the IEEE*, 103(3):409–423, March 2015.

[24] J. Mitola. Software radios-survey, critical evaluation and future directions. In *[Proceedings] NTC-92: National Telesystems Conference*, pages 13/15–13/23, May 1992.

[25] A. D. Olver. Compact antenna test ranges. In *1991 Seventh International Conference on Antennas and Propagation, ICAP 91 (IEE)*, pages 99–108 vol.1, April 1991.

[26] Sophocles J. Orfanidis. Electromagnetic waves and antennas. `https://www.ece.rutgers.edu/~orfanidi/ewa/ch22.pdf`, 2013. Accessed: 2010-02-11.

[27] Lee K. Patton and Brian Rigling. *A GNU Radio Based Software-Defined Radar.* [Dayton, Ohio] Wright State University, 2007., 2007.

[28] J. Pisane, S. Azarian, M. Lesturgie, and J. Verly. Automatic real-time collection of rcs of airplanes in a real bistatic low-frequency configuration using a software defined passive radar based on illuminators of opportunity. In *2012 IEEE Radar Conference*, pages 0950–0955, May 2012.

[29] A. Prabaswara, A. Munir, and A. B. Suksmono. Gnu radio based software-defined fmcw radar for weather surveillance application. In *2011 6th International Conference on Telecommunication Systems, Services, and Applications (TSSA)*, pages 227–230, Oct 2011.

[30] E. T. Rahardjo, E. Sandi, and F. Y. Zulkifli. Design of linear sparse array based on the taylor line source distribution element spacing. In *2017 IEEE Asia Pacific Microwave Conference (APMC)*, pages 61–64, Nov 2017.

[31] Theodore Rappaport. *Wireless Communications: Principles and Practice*. Prentice Hall PTR, Upper Saddle River, NJ, USA, 2nd edition, 2001.

[32] Jeff A. Sherman and Robert Jordens. Oscillator metrology with software defined radio. *REVIEW OF SCIENTIFIC INSTRUMENTS*, 87(5), n.d.

[33] Merrill I. Skolnik. History of radar, 2018.

[34] N. Ullah, Z. Huiling, T. Rahim, S. ur Rahman, and M. MuhammadKamal. Reduced side lobe level of sparse linear antenna array by optimized spacing and excitation amplitude using particle swarm optimization. pages 96–99, Oct 2017.

[35] John L. Volakis. *Antenna Engineering Handbook*. McGraw-Hill, 2007.

[36] Christian Wolff. Phased array antenna. `http://www.radartutorial.eu/06.antennas/Phased%20Array%20Antenna.en.html`. Accessed: 2019-02-10.